1 **High-precision atmospheric oxygen measurement comparisons between a newly built**

2 **CRDS analyzer and existing measurement techniques**

4 Tesfaye A. Berhanu[1,2], John Hoffnagle[2], Chris Rella[2], David Kimhak[2], Peter Nyfeler[1], Markus

5 Leuenberger[1]

6 [1]*Climate and Environmental Physics, Physics Institute and Oeschger Centre for Climate Change Research,*

7 *University of Bern, Bern, Switzerland*

8 [2]*Picarro Inc., 3105 Patrick Henry Drive, Santa Clara, CA, USA*

Abstract

11 Carbon dioxide and oxygen are tightly coupled in land-biospheres CO_2 - O_2 exchange

12 processes, while they are not coupled in oceanic exchange. For this reason, atmospheric

13 oxygen measurements can be used to constrain the global carbon cycle, especially oceanic

14 uptake. However, accurately quantifying the small (~1-100 ppm) variations in O_2 is

15 analytically challenging due to the very large atmospheric background which constitutes

16 about 20.9 % (~209500 ppm) of atmospheric air. Here we present a detailed description of the

17 analyzer and its operating principles as well as comprehensive laboratory and field studies for

18 a newly developed high-precision oxygen mixing ratio and isotopic composition analyzer

19 (Picarro G-2207) that is based on cavity ring-down spectroscopy (CRDS). From the

20 laboratory tests, we have calculated a short-term precision (standard error of one-minute O_2

21 mixing ratio measurements) of < 1 ppm for this analyzer based on measurements of eight

22 standard gases analyzed for two hours consecutively. In contrast to the currently existing

23 techniques, the instrument has an excellent long-term stability and therefore a calibration

24 every 12 hours is sufficient to get an overall uncertainty of < 5 ppm. Measurements of

25   ambient air were also conducted at the High-Altitude Research Station, Jungfraujoch and the

26   Beromünster tall tower in Switzerland. At both sites, we observed opposing and diurnally

27   varying CO_2 and O_2 profiles due to different processes such as combustion, photosynthesis

28   and respiration. Based on the combined measurements at Beromünster tower, we determined

29   height dependent O_2:CO_2 oxidation ratios varying between -0.98 to -1.60 , which increase

30   with the height of the tower inlet, possibly due to different source contribution such as natural

31   gas combustion with high oxidation ratio and biological processes which are at the lower end.

1. Introduction

33   Atmospheric oxygen comprises about 20.9 % of the global atmosphere and in the past decade

34   its concentration decreased at a rate of $\sim$ 20 per meg yr^{-1} (Keeling and Manning, 2014) mainly

35   associated with the increase in fossil fuel combustion. Measurements of atmospheric O_2 are

36   reported as the ratio to the N_2 concentration and expressed as $\delta(O_2/N_2)$ because the variations

37   in the concentrations of other atmospheric gases such as CO_2 can influence the O_2 partial

38   pressure while this ratio is insensitive to these changes in other gases. Atmospheric O_2 is

39   commonly expressed in units of per meg due to its small variability with respect to a large

40   background, where

$$\delta \left(\frac{O_2}{N_2}\right) (per\ meg) = \left(\frac{(\frac{O_2}{N_2})sample}{(\frac{O_2}{N_2})reference} - 1\right) . 10^6 \qquad (1)$$

42   Note that under the assumption the atmospheric N_2 content is constant (i.e. $N_{2sample}$ equals

43    $N_{2reference}$), we convert relative changes in oxygen given in per meg following equation 1 to

44   oxygen changes in parts per million (equivalent to micromol/mol) by multiplying by the O_2

45   mole fraction ($O_{2reference}$) expressed as 209500 ppm. (the O_2 mole fraction of atmospheric air)

46   (Machta and Hughes, 1970). Hence 1 ppm corresponds approximately to 4.8 per meg, or 1 per

47   meg to 1/4.8 (209500/10^6) ppm

In contrast to O_2, the global average atmospheric CO_2 mixing ratio increased to 405.0 ppm averaged over 2017 since its preindustrial value of 280 ppm (Le Quéré et al., 2017). As the variability of atmospheric oxygen is directly linked to the carbon cycle, both its short and long-term observations can be used to better constrain the carbon cycle. For example, since first suggested by Keeling and Shertz (1992) the long-term trends derived from concurrent measurements of atmospheric CO_2 and O_2 have been widely used to quantify the partitioning of atmospheric CO_2 between the land-biosphere and oceanic sinks (Battle et al., 2000; Goto et al., 2017; Manning and Keeling, 2006; Valentino et al., 2008). This method hinges on the linear coupling between CO_2 and O_2 with an oxidation ratio (OR, defined as the stoichiometric ratio of exchange during various process such as photosynthesis and respiration expressed using α) of 1.1 for the terrestrial biosphere photosynthesis-respiration processes (α_b) and 1.4 for fossil fuel combustion (α_f) while they are decoupled for oceanic processes (α_o = 0). Meanwhile, the short-term variability in atmospheric oxygen can be used to estimate marine biological productivity and air-sea gas exchange (Keeling et al., 1998; Nevison et al., 2012). However, the accuracy of these estimates is primarily linked to the accuracy and precision of atmospheric O_2 measurements and the assumed ORs for the different processes which are highly variable in contrast to atmospheric CO_2 that can be well measured within the precision guidelines set by the Global Atmospheric Watch (GAW) ($\pm$ 0.1 ppm for the northern hemisphere).

Currently there are several, mostly custom built techniques that can measure atmospheric O_2 variations as oxygen concentration based on interferometric, paramagnetic, UV absorption and fuel cell technology (Keeling, 1988a; Manning et al., 1999; Stephens et al., 2007) or as O_2/N_2 ratios to account for the large background effect using gas chromatography with thermal conductivity detector (GC-TCD) or gas chromatography

coupled to mass spectrometry (GC-MS) (Bender et al., 1994; Tohjima, 2000). Despite the fact that these techniques have been used for more than two decades, accurate quantification of atmospheric oxygen variability remains challenging primarily because the small ppm-level atmospheric oxygen signal rides on a ~ 210,000 ppm background, which places stringent requirements on the precision and drift of the analysis methods especially for continuous monitoring(note that the GAW recommendation for the measurement precision of O_2/N_2 is 2 per meg). The techniques listed above struggle to routinely achieve the necessary performance for various reasons, including i) instability over time that requires frequent measurement interruption for calibration, ii) measurement bias with ambient and sample temperature and/or pressure, and/or iii) systematic errors in the measurement due to other atmospheric species. Further, some techniques require the use of consumables and rely on high vacuum, which complicates field deployment.

In this manuscript we describe a new high precision oxygen concentration and isotopic composition analyzer by Picarro Inc., Santa Clara, USA (G-2207) based on CRDS technology. Here, we will introduce the analyzer design principles in details, describe the unique features of the analyzer and evaluate its performance based on various independent laboratory and field tests by comparing it with currently existing techniques. Then, we will present and interpret our observations based on field measurements. Finally, we will conclude its overall performance and provide recommendations and possible improvements.

2. Analyzer design principles

The analyzer described here is derived from the Picarro G2000 series of CRDS analyzers. The basic elements have been described elsewhere (Crosson, 2008; Martin et al., 2016; Steig et al., 2014): briefly, the instrument is built around a high-finesse, traveling-wave optical cavity, which is coupled to either of two single-frequency Distributed FeedBack-

96   stabilized semiconductor lasers. One cavity mirror is mounted on a piezoelectric translator

97   (PZT) to allow fine tuning of the cavity resonance frequencies. A semiconductor optical

98   amplifier between the laser sources and the cavity boosts the laser power and serves as a fast-

99   optical switch. The cavity body is constructed of invar and enclosed in a temperature

100   stabilized box (T = 45° C, stabilized to approximately 0.01 °C) for dimensional and

101   spectroscopic stability. A vacuum pump pulls the gas to be sampled through the cavity and a

102   proportional valve between the cavity and the pump maintains the sample pressure in the

103   cavity at a value of 340 hPa, with variations on the order of 1 Pa. The instrument has a

104   wavelength monitor, based upon measurements of interference fringes from a solid etalon,

105   which is used to control the laser wavelength by adjusting the laser temperature and current.

106   The wavelength monitor is a fiber-coupled device located between the laser and the cavity. A

107   fraction of the beam from the input fiber is collected using a beam splitter for the wavelength

108   measurement and the remaining power is collected in the output fiber. A high-speed

109   photodiode monitors the optical power emerging from the cavity. The instrument's data

110   acquisition system is used to sweep the laser frequency over the spectral feature to be

111   measured, modulates the laser output to initiate ring-downs, and fits the ring-down signal to

112   an exponential function to generate a spectrogram of optical loss versus laser frequency. For

113   this instrument the empty cavity ring-down time constant is about 39 μs. Subsequent program

114   modules compare the measured loss spectrum to a spectral model, using non-linear least-

115   squares fitting (Press et al., 1986) to find the best-fit model parameters and thereby obtain a

116   quantitative measure of the absorption due to the target molecule, and finally apply a

117   calibration factor to the optical absorption to deduce the molecular concentration. When

118   operating in its normal gas analysis mode, the instrument acquires about 200-300 ring-downs

119 per second and achieves a noise equivalent absorption of typically about 10^{-11} cm^{-1} Hz$^{-1/2}$,

120 with some variation between instruments.

121   The primary goal when designing this analyzer was to measure the molecular oxygen

122 concentration with few-per-meg level precision and stability. In this context operational

123 stability is as important as signal-to-noise. Our experience has been that the most stable

124 operation of the analyzer is achieved when the optical phase length of the cavity is held as

125 nearly constant as possible. In this case the free spectral range (FSR, 0.0206 cm^{-1}) of the

126 temperature stabilized, invar ring-down cavity provides a better optical frequency standard

127 than the etalon-based wavelength monitor, which in turn allows more consistent

128 measurements of absorption line width and integrated absorption line intensity (Steig et al.,

129 2014). For a small, field-deployable instrument, it is not practical to stabilize the absolute

130 frequencies of the cavity modes to an optical frequency standard (Hodges et al., 2004) but the

131 oxygen lines themselves, under conditions of constant temperature and pressure, provide an

132 adequate frequency reference. The oxygen spectrum was also used to calibrate the FSR, by

133 comparing a wide (approximately 10 cm^{-1}) FSR-spaced spectrum with the Hitran database

134 (Rothman et al., 2013).

135   To determine molecular oxygen concentration, the analyzer measures absorption of the

136 Q13Q13 component of the $a^1\Delta_g \leftarrow X^3\Sigma^-_g$ band, at 7878.805547 cm^{-1}, according to the latest

137 edition of Hitran (Gordon et al., 2017). This is one of the strongest near-infrared lines of

138 oxygen, well separated from other oxygen lines, and reasonably free of spectral interference

139 from water, carbon dioxide, methane, and other constituents of clean air. The spectral model

140 for this line was developed using reference spectra of clean, dry, synthetic air that were

141 acquired with the same hardware as in the field-deployable analyzer, but with special-purpose

142 software that allows it to operate as a more general spectrometer.

143   Recently, considerable work has been done to advance the understanding of spectral

144   line shapes and to define functional representations that better describe the processes that

145   determine spectral line shapes than does the Voigt model (Hartmann et al., 2008; Tennyson et

146   al., 2014, Tran et al., 2019). Line shape studies have been published for the 1.27 μm band of

147   O_2 (Fleisher et al., 2015; Lamouroux et al., 2014), though not to our knowledge for the Q

148   branch. The apparatus used here is not capable of spectroscopic studies of comparable

149   precision; the absolute temperature and pressure monitoring and especially the frequency

150   metrology are far too crude for that purpose. Our goal is merely to define a simple model of

151   the Q13Q13 line that is adequate for least-squares retrievals of the O_2 absorption under the

152   limited range of conditions (stabilized temperature and pressure) that the operational analyzer

153   experiences in the field. The CRDS analyzers use the Galatry function (Varghese and Hanson,

154   1984), which is distinctly better than the Voigt and still easily and quickly evaluated for line

155   shape modeling. Ultimately, the usefulness of the spectral model is to be evaluated by the

156   precision and stability of the O_2 measurements when compared with established techniques.

157   For spectral model development, this spectrometer has the drawback that the cavity FSR, is

158   too large to reveal much detail of the absorption line shape, even with the simplifying

159   assumption of a Galatry line shape. We therefore acquired a set of four interleaved spectra,

160   with the PZT-actuated mirror moved to offset the cavity modes of the individual FSR-spaced

161   spectra by one-fourth of an FSR. The precise offsets were determined from fits to the strong

162   and well-isolated O_2 lines in the spectra. From the consistency of the fitted line centers, we

163   estimate that the positioning of the interleaved spectra was accurate to approximately 10

164   MHz. The spectrum of the Q13Q13 line acquired in this manner is shown in Figure 1,

165   together with the best-fit Galatry function. It stands out that the residuals are largely odd in

166   detuning from the line center: this shows the limitations of the Galatry model in this case,

167 since the Galatry function is purely even about the line center. The shape of the absorption

168 line in this model is specified by two dimensionless parameters: the collisional broadening

169 parameter

170 $y = \gamma/\sigma_D$ (2)

171 and the collisional narrowing parameter

172 $z = \beta/\sigma_D$ (3)

173 where γ is the frequency of broadening transitions, β is the velocity change collision rate, and

174 σ_D is the 1/e Doppler half-width of the transition, given by

175 $\sigma_D = \nu_0(2k_BT/Mc^2)^{1/2}$ (4)

176 where ν_0 is the transition frequency, k_B is Boltzmann's constant (J. K^{-1}), T is the sample

177 temperature (K), M is the molecular mass (amu), and c is the speed of light (m/s). Figure 2

178 shows the values of y and z obtained from spectra acquired in the same way as Figure 1, as a

179 function of cavity pressure. The values depend linearly on pressure, as expected from the

180 Galatry model, but the unconstrained linear fits do not go precisely through the origin. It is

181 not clear whether this represents a breakdown of the Galatry model or simply reflects the

182 limited quality of the data set. The slope of y can be converted to an air-broadened collisional

183 width $\gamma_{air} = 0.0442$ cm^{-1}/atm, which agrees with the Hitran value of 0.0460 cm^{-1}/atm (Gordon

184 et al., 2016) to within the uncertainty estimate stated by Hitran (uncertainty code 4 for γ_{air}

185 corresponding to 10% --20% relative uncertainty). The slope of z can be interpreted in terms of

186 the optical diffusion coefficient (Fleisher et al., 2015), yielding D = 0.285 cm^2 s^{-1}, compared

187 to the literature value of 0.233 cm^2 s^{-1} for O_2 in air at 45 °C (Marrero and Mason, 1972).

188 Although the anticipated use of the analyzer is for ambient air samples having a very small

189 range of O_2 concentrations, we did investigate the variation of the line shape in binary

190 mixtures of O_2 and N_2 shown in Figure 3. The error bars are taken from the output of the

191   Levenberg-Marquardt fitting routine (Press et al., 1992). The dependence of the collisional

192   broadening parameter z on O_2 mole fraction was considered too small to be significant, but

193   the variation in y was used in the subsequent analysis of the air samples. Note that Wójtewicz

194   et al. (Wójtewicz et al., 2014) also found collisional broadening coefficients for nitrogen to be

195   slightly larger than for oxygen in measurements of one O_2 line in the B-band.

196   The primary goal in designing the analyzer was to achieve high enough precision to

197   make meaningful measurements of O_2 in clean atmospheric samples. Although the current

198   best practice for such high-precision measurements is to work with dried samples, we decided

199   to include high precision measurements of water vapor. There were two reasons for this

200   decision: one is to serve as a monitor for residual water vapor, which is difficult to remove

201   completely from the ring-down cavity and associated sample handling hardware, and the

202   second and more ambitious reason was to see how well the effect of water vapor could be

203   corrected for measurements of undried ambient air. While it was considered unlikely that

204   measurements of undried air could compete in accuracy with those of dried air, it might be

205   possible to correct for water vapor well enough to enable useful measurements in some

206   circumstances without the expense and inconvenience of drying the sample. For this purpose,

207   a second laser was added, which probes the $7_{1,6} \rightarrow 8_{4,5}$ component of the $2v_3$ band of water

208   vapor, at of 7816.75210 cm^{-1} (Gordon et al., 2017). The Galatry model was used to fit spectra

209   of synthetic air humidified to various levels of water vapor concentration. These fits also

210   included two other nearby, very weak water lines, with intensities less than 1% of the strong

211   transition, in order that their absorption should not perturb the line shape of the main

212   transition. Results for the shape of the 7816.75210 cm^{-1} line are shown in Figure 4. At the

213   level that we can measure, only the y-parameter has a meaningful variation with water

214   concentration. From the linear fit one obtains a pressure broadening coefficient for air, $\gamma_{air} =$

215 0.0752 cm^{-1}/atm, in reasonable agreement with the Hitran value γ_{air} = 0.0787 cm^{-1}/atm

216 (Gordon et al., 2017), and a self-broadening coefficient γ_{self} = 0.413 cm^{-1}/atm, to be compared

217 with the Hitran value γ_{self} = 0.366 cm^{-1}/atm. Since the uncertainty estimate for the Hitran

218 values is 10 % to 20 %, this level of agreement seems reasonable.

219   We also looked at absorption from water near the Q13Q13 absorption line of O_2.

220 These spectra were measured in a background of pure nitrogen to reveal the very weak lines

221 interfering with the O_2 measurement. Without the strong O_2 lines, it was impossible to

222 interleave FSR-spaced spectra, so in this case the frequency axis comes from the analyzer's

223 wavelength monitor. The upper panel of Figure 5 shows the spectrum of saturated water vapor

224 in nitrogen, together with a fit to a Voigt model of the molecular lines. The measurement was

225 made at a pressure of 340 hPa and temperature of 45° C. The main features are the Q13Q13 line

226 from trace contamination of oxygen in the sample and several lines that arise from normal water

227 ($^1H_2^{16}O$) and deuterated water ($^1H^2H^{16}O$ also abbreviated HDO). The lower panel of Figure 5 shows

228 the lines tabulated in Hitran. Immediately after the data in Figure 5 were acquired,

229 measurements were also made at 7816.85210 cm^{-1}, to establish the relationship between the

230 absorption strengths in the two spectral regions. The relative intensities of the H_2O and HDO

231 lines change with variations in the isotopic composition of the water, but fortunately the direct

232 interference with the oxygen Q13Q13 lines comes entirely from the H_2O isotopologue, with

233 the strongest HDO line being separated by approximately 8 line widths (FWHM) from the

234 Q13Q13 line. Hitran simulations for molecules other than water that are expected to be

235 present in clean, ambient air indicate that direct interference with the Q13Q13 line should be

236 negligible at the level of precision considered here. In the case of CO_2, the dilution of oxygen

237 due to 400 ppm of CO_2 is significant, and larger than any direct spectral interference.

238   Finally, we investigated the influence of water vapor on the shape of the O_2 Q13Q13

239   line. Switching between the two lasers sources, we acquired FSR-spaced spectra of

240   humidified synthetic air, alternately covering the 7817 cm^{-1} and 7878 cm^{-1} regions. Individual

241   spectra were acquired in less than 2 s, so changes in water vapor concentration between

242   spectra were small. These spectra, with frequency resolution of 0.0206 cm^{-1}, were analyzed by

243   nonlinear least-squares fitting with the following spectral models: the 7817 cm^{-1} spectra were

244   modeled as the sum of an empty-cavity baseline having an adjustable offset level and slope

245   and the water spectrum is modeled with three peaks: one strong line and two weak perturbers.

246   The molecular absorption of the main peak was expressed as an adjustable amplitude, A_w,

247   multiplying a dimensionless, area-normalized Galatry function (Varghese and Hanson, 1984).

248   The weak perturbers were modeled by Voigt profiles with amplitudes and line widths that

249   were constrained to be in fixed proportions to the strong line, and therefore added no new

250   degrees of freedom to the fitting procedure. Since the amplitude A_w multiplies an area-

251   normalized shape function, it is essentially equivalent to the area of the absorption line, to the

252   extent that the Galatry model provides a valid description of the line shape. The Doppler

253   width of the Galatry function was fixed based on the measured cell temperature, the y-

254   parameter was allowed to vary, and the z-parameter was constrained to be proportional to y,

255   based on measurements summarized in Figure 2. In addition, the center frequency of the

256   Galatry function was adjusted to match the data set, giving a total of five free parameters for

257   this fit. The 7878 cm^{-1} spectra were modeled with an adjustable baseline offset and slope and

258   molecular absorption amplitude, A_{O2}, describing the Q13Q13 O_2 line. Here, too, the y-

259   parameter and line center position of the O_2 lines were allowed to adjust, and the z-parameter

260   was constrained to be proportional to y. The weak water lines interfering with oxygen

261   absorption were included in the model, but with no additional free parameters; rather the

262 amplitudes were preset based on the measured water absorption at 7817 cm^{-1} and the

263 previously determined amplitude relationships between the water lines. This procedure does

264 not account for variations in HDO abundance, which may introduce some systematic error

265 into the water vapor correction for samples of unusual isotopic composition, but it should

266 accurately model the most important lines that interfere with the oxygen measurement.

267 Collisional broadening of the Q13Q13 O$_2$ line by water vapor is shown in Figure 6. From the

268 linear fit one obtains a coefficient for collisional broadening of the Q13Q13 line by water

269 vapor of γ_{water} = 0.0442 cm^{-1}/atm at 45 °C. Recently, parameters describing broadening of

270 oxygen lines by water vapor, obtained by empirical modeling of selected experimental

271 data, were added to the Hitran data base (Tan et al., In review). The new Hitran entries predict

272 a value of 0.0486 cm-1/atm at 45 °C, which is in agreement with our measurement within the

273 5-10% uncertainty attributed by Hitran to the broadening parameter. The alternating

274 measurements at 7817 cm^{-1} and 7878 cm^{-1} also calibrated the relationship between water mole

275 fraction and the absorption at 7817 cm^{-1}, using a dilution analysis described by Filges et al.

276 (2018), who showed that the results obtained this way agree well with water vapor fractions

277 measured with a conventional hygrometer. Figure 7 shows the measured amplitudes of the

278 water and oxygen lines for samples of variable humidity. Since the air came from a tank of

279 constant composition, the oxygen concentration changes due to dilution of oxygen when

280 water is added. Assuming that this is the sole cause of the change in measured absorption,

281 since the line shapes were being constantly adjusted to account for changes in collisional

282 broadening, it is straightforward to deduce the relation between the water fraction and the

283 absorption amplitude. This calibration was used to generate the water fraction axes in Figures

284 4 and 6. We note that we did not take particular care to control or measure the quantity of

285 dissolved gases, especially oxygen and carbon dioxide, in the water used for this experiment.

286 While these gases would not significantly affect the water calibration, they may affect the

287 water vapor correction of the oxygen measurement at the ppm level. More work needs to be

288 done to investigate the water vapor correction of the oxygen measurement.

289 The observations described above were used to design a method to measure oxygen

290 concentration in ambient air. Gas from the inlet to the analyzer is drawn through the cavity at

291 a rate of about 100 sccm (standard cubic centimeter per minute) and the conditions in the

292 cavity are held stable at 340 hPa and 45°C. In its analysis mode the analyzer alternately

293 measures ring-downs in the 7817 cm^{-1} and 7878 cm^{-1} regions. At 7878 cm^{-1} measurements are

294 made at 11 different frequencies, spaced by one FSR of the cavity and centered at the peak of

295 the Q13Q13 line. Multiple ring-down measurements are made to improve the precision of the

296 loss determination, with a total of 305 ring-downs allocated to one spectrum. In the 7817 cm^{-}

297 ^{1} region measurements are also made at 11 distinct frequencies at FSR spacings. Only 35 ring-

298 downs are allocated to this spectral region, since the measurement of O_2 is much more

299 important than water vapor. The data sets are analysed using a Levenberg-Marquardt fitting

300 routine, which adjusts five free parameters in each region to find the best agreement to a

301 spectral model based on Galatry line shapes, as described above. One of the outputs of the

302 7878 cm^{-1} fit is the frequency offset of the FSR grid from the center of the Q13Q13 line. This

303 information is used to adjust the position of the PZT actuated mirror to keep the

304 measurements centered on the line, effectively stabilizing the optical path length of the cavity

305 to the frequency of the O_2 line. The reported water fraction is obtained by multiplying the

306 fitted amplitude of the water line by a calibration constant derived from the dilution

307 experiment as explained above. For the O_2 fraction a slightly more complicated procedure is

308 followed. It was observed that the least-squares fitting of the data gives highly correlated

309 results for the amplitude of the absorption line and the line width parameter y. The correlation

310   may be due in part to covariance of the fitted amplitude (proportional to line area) and line

311   width (Press et al., 1992) and it may also have a contribution from pressure variations that the

312   pressure sensor is unable to detect. The ratio A_{O2}/y can be determined from the fit much more

313   precisely than A_{O2} alone and so gives a more sensitive measurement of molecular absorption.

314   It also has the advantage of being independent of sample pressure, to the extent that the

315   Galatry model applies (Figure 2). However, using the ratio A_{O2}/y as a metric for absorption

316   adds more complications if measurements are to be made over a range of O_2 and water

317   concentrations, because the O_2/ N_2 ratio and the water concentration affect the line width

318   independently of pressure and O_2 concentration alone. To minimize systematic errors due to

319   these broadening effects, we define a nominal y-parameter based on the measured amplitudes

320   of the O_2 and water lines and the line broadening dependences shown in Figures 3 and 4. The

321   measured ratio A_{O2}/y is multiplied by the nominal y to obtain a quantity that is ideally

322   independent of pressure and water concentration, and this is the quantity that is multiplied by

323   a calibration constant to give the reported O_2 fraction. In addition, a dry mole fraction is

324   reported for O_2, defined as the directly measured mole fraction corrected for water dilution.

325   The main goal in developing this instrument was to make high precision

326   measurements of O_2 mole fraction, based on absorption by the dominant $^{16}O_2$ isotopologue.

327   The absorption lines of the rarer isotopologues are also present nearby, so a mode of operation

328   was included in which one laser is scanned over neighboring lines of $^{16}O_2$ and $^{16}O^{18}O$ and the

329   ratio of amplitudes is used to derive an isotopic ratio, reported in the usual delta notation. In

330   this case the operating pressure was reduced to 160 hPa to improve the resolution of the

331   nearby lines. The lines measured were the Q3Q3 line of $^{16}O_2$, at 7882.18670 cm^{-1}, and the

332   Q9Q9 line of $^{16}O^{18}O$, at 7882.050155 cm^{-1}. The measurement procedure is very much like

333   that for the O_2 fraction measurement, so it will not be described in detail, only the main

334 differences will be noted. One is that in determining an isotopic ratio, normalizing absorption

335 amplitudes by line widths does not provide any advantage, instead we simply take the ratio of

336 amplitudes to compute delta. Although the Q9Q9 line and its neighbor Q8Q8 are the strongest

337 ones in this band, absorption by $^{16}O^{18}O$ is still very weak, only about 5×10^{-9} cm^{-1} at the line

338 center under the conditions we used. The signal-to-noise that can be achieved with this

339 analyzer is not adequate to determine both the amplitude and the width of the $^{16}O^{18}O$ line with

340 useful precision, so in the fitting step the y-parameter of the $^{16}O^{18}O$ line is constrained to be a

341 constant factor times the fitted y-parameter for the $^{16}O_2$ line. Additionally, because of the

342 weakness of the rare isotopologue absorption, the majority of ring-downs in each spectrum is

343 devoted to measuring $^{16}O^{18}O$ i.e. 232 ring-downs in each spectrum versus only 40 for $^{16}O_2$.

344 This implies that the mole fraction measurement in the isotopic mode is much less precise

345 than when the analyzer measures the Q13Q13 line alone.

346 **3. Results and Discussions**

347 **3.1. Laboratory tests at Picarro, Santa Clara**

348 3.1.1. Temperature and pressure sensitivity

349 One set of tests was done to determine how well the goal was met of minimizing the

350 susceptibility of the concentration measurements to noise or drift of the sample temperature

351 and pressure. For these tests the analyzer sampled dry synthetic air from a tank and the

352 temperature and pressure setpoints of the cavity were adjusted upward and downward from

353 the nominal values, to obtain an estimate of the differential response. We express the

354 sensitivity to experimental conditions in relative form, that is the derivative with respect to

355 temperature or pressure divided by the signal under nominal conditions.

356 From these experiments, we determined a temperature sensitivity of -2.1×10^{-4} K^{-1} and

357 a pressure sensitivity of $+9.8 \times 10^{-6}$ hPa^{-1}. The temperature sensitivity is somewhat larger than

358 expected based on a calculation using Hitran data to estimate the temperature dependences of

359 all the quantities that go into the measured absorption of the Q13Q13 line. The pressure

360 sensitivity is strikingly small, indicating a good cancelation of the pressure dependence of

361 absorption amplitude and line width. Both temperature and pressure sensitivities are small

362 enough to have a negligible effect on short-term precision of measurements made with the

363 stabilized ring-down cavity, though long-term drifts in the sensors are always a matter of

364 concern.

365 3.1.2. Measurement precision and drift

366   Measurement precision was evaluated by analyzing synthetic air containing nominal

367 atmospheric concentrations of CO_2 and CH_4 from an aluminum Luxfer cylinder over a period

368 of several days. The tank, oriented horizontally and thermally insulated (though not

369 controlled), was connected directly to the instrument (S/N TADS2001) with a 2-stage

370 pressure regulator and stainless-steel tubing with an additional orifice to about 55 sccm. For

371 the isotopic mode of operation, the precision of the measurement was also tested by making

372 repeated measurements from a tank of clean, dry synthetic air.

373   Figure 8 shows the time series of the precision test data, displaying the reported

374 oxygen concentration, the height of the oxygen absorption peak, the width of the oxygen

375 absorption peak and the ambient temperature. The residual error of the analyzer, although

376 small, is nevertheless significant given the stringent targets set forth by the WMO-GAW

377 program. Possible sources of error include: temperature drifts due to sensor drift or gradients;

378 pressure errors due to sensor drift; optical artifacts such as parasitic reflections, higher order

379 cavity mode excitation, and/or loss nonlinearity that can distort the reported oxygen spectrum.

380 More work is required to identify and eliminate these small drifts.

381   The Allan standard deviation of the reported O_2 fraction is shown in the Allan-Werle

382   plot in Figure 9. The ordinate on this plot is the square root of the Allan variance of reported

383   mole fraction, so 1 ppm in these units corresponds to about 5 per meg in the ratio of O_2/ N_2.

384   The precision of averaged measurements improves as $\tau^{-1/2}$ for approximately 5000 s and

385   reaches 1 ppm in less than 10 minutes and remains below 1 ppm for time scales on the order

386   of about 1 hour (τ is the averaging time which is the abscissa of the Allan-Werle plot).

387   Figure 10 shows the precision of $\delta(^{18}O)$ (uncalibrated) derived from the ratio of lines

388   measured at 7882 cm^{-1}. Because of the weak signal from the $^{16}O^{18}O$ line, it is necessary to

389   average for more than 20 seconds or more to achieve 1‰ precision on the isotopic ratio. As

390   for the concentration measurement, averaging improves the measurement precision for time

391   scales up to about 1 hour.

392   **3.2. Laboratory measurements at the University of Bern**

393   3.2.1. Measurements of standard gases

394   The performance of the instrument was tested by analyzing eight standard gases with

395   precisely known CO_2 and O_2 compositions (Table 1) using the CRDS analyzer and comparing

396   it to parallel measurements with a paramagnetic oxygen sensor (PM1155 oxygen transducer,

397   Servomex Ltd, UK) embedded to a commercially available fuel cell oxygen analyzer

398   (OXZILLA II, Sable Systems International, USA) (Sturm et al., 2006) as well as with an

399   isotope ratio mass spectrometer (IRMS, Finnigan Delta^{Plus}XP). The design of the

400   measurement set-up is shown in Figure 11. Standard gases were directly connected to the

401   pressure controlling unit, and a multi-port valve (V2) was used to select among the standard

402   gases. Flow from each cylinder was adjusted to about 120 sccm which was eventually

403   directed to a selection valve (V1), allowing switching between ambient air and standard gases.

404   Flow towards and out of the fuel cell analyzer was controlled by the pressure controlling unit.

The O_2 mixing ratio of this incoming gas was first measured on the Paramagnetic O_2 sensor and then directed towards a non-dispersive infrared analyzer (NDIR) (Li-7000, LICOR, USA) for measuring CO_2 and H_2O. The outflow from this analyzer (100 sccm) returns to the pressure controlling unit and was eventually divided between the CRDS analyzer (which uses about 75-80 sccm) and the IRMS (~ 20 sccm) via a Tee-junction. Each cylinder was measured for two hours in each system controlled by a LabView program.

First, we investigated the influence of this Tee-junction, which splits the gas flow between the CRDS and the IRMS, on the measured O_2 values. Manning (2001) showed that the fractionation of O_2 in the presence of a Tee-Junction is strongly dependent on the splitting ratios as well as temperature and pressure gradients. Hence, we measured and compared the O_2 mixing ratios of two standard gases (CA07045 and CA060943) in two cases: i) in the presence of a Tee-junction with different CRDS to IRMS splitting ratios and ii) without a Tee-junction so that all gas flow is directed towards the CRDS analyzer. The splitting ratios in these test experiments vary from 1:1 to 1:100, and reversed to change the major flow direction either to the CRDS or the IRMS. Note that the experimental condition in this manuscript is with a 4:1 splitting ratio (i.e. ~ 80 sccm towards the CRDS analyzer and ~ 20 sccm towards the IRMS).

In the cases of the smaller splitting ratios (1:1, 1:4 and 4:1), which are relevant for the results presented in this study, only minor differences in the measured O_2 mixing ratios were observed when compared to case ii (i.e. without a Tee-junction). For these two cylinders measured, the average differences in these cases were about 0.5 ppm, calculated as the mean of the differences in the raw O_2 measurements of the last 60 seconds. The negligible fractionation can indeed be the result of smaller splitting ratios while strong influence is usually expected in case of larger splitting ratios (Stephens et al., 2007). For higher splitting

429 ratios, the result seems inconclusive without any dependence on the ratios due to the strong

430 decline in the cylinder temperature (specifically at the pressure gauge) caused by higher flow

431 to achieve the higher splitting ratios (as high as 1:100). Hence, these tests need to be

432 conducted in a temperature-controlled condition and the results could not be discussed in this

433 manuscript.

434   Figure 12 shows the standard gas measurements for the seven cylinders with known

435 CO_2 and O_2 mixing ratios (Table 1) using both the CRDS and the Paramagnetic analyzers.

436 Standard eight, which has too high O_2, is not shown in the figure as the figure is zoomed-in to

437 better illustrate the change in O_2 for the remaining cylinders. While the first five cylinders

438 contain O_2 and CO_2 mole fractions comparable to ambient air values, standards 6 & 8 had

439 either very low or very high O_2, respectively. In addition, standards 6 and 7 have very low and

440 very high CO_2 mixing ratios. Note that due to its very high CO_2 content (~ 2700 ppm),

441 standard 7 was not measured on the IRMS and hence the O_2 mixing ratio is unknown. The

442 measured mixing ratios for the six standard gases measured with the two systems are in very

443 good agreement while cylinder 7 showed an opposing signal for the two analyzers compared

444 to standard 6 (Figure 12). While the Paramagnetic analyzer showed a higher O_2 mixing ratio,

445 the values from the CRDS analyzer are lower in O_2. This can be associated with the very high

446 CO_2 mixing ratio in standard 7, which leads to a strong dilution effect in the CRDS analyzer

447 as it does not include any correction function for dilution effect from CO_2. However, such

448 high CO_2 mixing ratios may not be that important for most atmospheric research. Yet, it

449 should be considered to include a parallel CO_2 mixing ratios measurement to the instrument

450 as it will further improve the accuracy. This would be especially important for biological or

451 physiological studies where a wide range of CO_2 and O_2 concentrations must be expected.

452   The measurement precision of the CRDS analyzer was calculated as the standard error

453   of the mean i.e. the standard deviation (1-σ) of the last 1-minute raw measurements divided

454   by the square root of the number of measurements ($n = 60$), and for all these cylinders the

455   values are usually between 0.5 ppm to 0.7 ppm. For parallel measurements of these cylinders

456   using a Paramagnetic analyzer, we obtained a precision of about 1 ppm, calculated exactly the

457   same way.

458   We also made a correlation plot to see which of the two instruments are in better

459   agreement with the assigned values based on IRMS measurements for the individual

460   cylinders. While similar correlation coefficients were observed for both analyzers, different

461   slopes were calculated (Fig. A.1). This is due to the fact that the IRMS measures the O_2 to N_2

462   ratio ($\delta(O_2/N_2)$) in per meg, while the CRDS and the Paramagnetic analyzers provide non-

463   calibrated O_2 mixing ratios in units of ppm and per meg, respectively. If we exclude the two

464   standard gases with the highest and lowest O_2 mixing ratios (standards 7 and 8) that are

465   subjected to strong dilution effects, both the slope and the r^2 values decrease from those

466   shown in Figure A.1. But this decrease is larger in the case of the Paramagnetic

467   measurements, implying a slightly better linearity of the CRDS analyzer.

468   3.2.2. Measurements of ambient air

469   Ambient air measurements were conducted from the roof top of our laboratory at the

470   University of Bern to evaluate the analyzer's performance under atmospheric variability.

471   Ambient air was continuously aspirated from the inlet at the roof of the building at a flow rate

472   of ~ 250 sccm which is then dried using a cooling trap kept at -90 °C towards the switching

473   valve (V1) and measured in similar way to the standard gases as explained above. The

474   measurement values obtained here were compared with the parallel measurements by the

475   Paramagnetic sensor to test the instruments stability and accuracy.

476   Figures 13 panels a &b show the 1-minute average ambient air measurements from the

477   rooftop inlet by the Paramagnetic and the CRDS analyzers at the beginning of the testing

478   period including standard gases measured every 12-hour. While the Paramagnetic analyzer

479   seems to be stable, the CRDS analyzer showed a strong drift for an extended period. This can

480   be due to unstable conditions in the CRDS measurement system as it started operating right

481   after it was unpacked. Hence, we looked into temperature inside the instrument chassis and

482   pressure records, which were stable within the manufacturer's recommended range during this

483   period. As the CRDS analyzer incorporates a water correction function, interference from this

484   species should be well accounted. Even comparing the analyzer's parallel water

485   measurements to water measurements by the NDIR system such a drift was not observed. It

486   should be noted that the two internal standard gases which were less frequently measured

487   (every 12 hours) during this period were also drifting following similar pattern. This implies

488   that the drift is associated with the analyzer. Interestingly, this pattern can be modeled using a

489   polynomial function which can then be used to correct for the observed drift in the ambient air

490   measurements. After applying a polynomial drift correction, we were able to fully accounted

491   for the observed drift. However, the manufacturer decided to further investigate possible

492   causes of this drift. After further improvements, we obtained the first commercial analyzer in

493   September 2017 and repeated the above tests (Figure 13 c &d). No such drift was observed

494   any more in the standard gases or in ambient air measurements.

495   We believe that the optical amplifier has caused the drift in the first system and not anymore

496   included in the design of the product which produced a significant amount of broadband light

497   that could fill the cavity (albeit with a low coupling coefficient), and would ring down with a

498   different (and generally much faster) time constant that the baseline loss of the cavity.

499   However, the ringdown time on the peak of the oxygen line is just 10 microseconds, such that

500   the broadband light might have distorted the single exponential decay of the central laser

501   frequency, leading to the observed drift in the oxygen signal. However, we were not able to

502   confirm this hypothesis.

503   3.2.3. Water correction test

504   Measurements of oxygen are reported as both wet ($O_{2,\ raw}$) and dry ($O_{2,\ dry}$) mole

505   fractions by the CRDS analyzer as it also measures water vapor in parallel at its water

506   absorption line (7817 cm^{-1}), and corrects for the dilution effect based on an inbuilt numerical

507   function:

508    $$O_{2,dry} = \frac{O_{2,raw}}{1 - H_2O}$$ (5)

509   where H_2O is the measured water mole fraction.

510   The efficiency of water correction by this function was assessed in two ways: i) by comparing

511   the water vapor content in standard air measured by this analyzer with similar measurements

512   by the NDIR analyzer and ii) by comparing the oxygen mixing ratios between non-dried

513   ambient air measured and corrected for water dilution by the CRDS analyzer with dried air

514   measured using a paramagnetic analyzer.

515   Figure 14 shows the water vapor content for standard gases measured continuously for

516   two days by the CRDS and the NDIR analyzers. Note that the two data sets are manually

517   fitted to each other as the measured water values by the NDIR analyzer are not calibrated.

518   Based on this plot, the two analyzers are in very good agreement although there are small

519   differences during very dry conditions (low water content).

520   Figure 15a shows the dried ambient air water measurements in both analyzers with

521   frequent spikes due to valve switching while measuring standard gases. In the second case,

522   where the water trap was by-passed and non-dried air was allowed to the CRDS analyzer

523   keeping the dried air flow to the NDIR (Figure 15b), a clear increase in the water

524   measurements in the CRDS analyzer can be observed. Here, it should be noted that there are

525   no spikes in the water measurements of the CRDS analyzers as there are no standard gas

526   measurements in between and the inlet is directly connected to the CRDS analyzer (Figure

527   11). Figures 15c & 15d show the difference in oxygen measurements of ambient air measured

528   in both analyzers in the two cases stated above (note that the CRDS uses its built-in water

529   correction function applying Eq. 5). The measurements of the Paramagnetic analyzer were

530   scaled to ppm units by applying the correlation equation obtained from the six standard gas

531   measurements of the two analyzers (Fig. A.1). Note that the CRDS measurements were

532   corrected for the observed drift using the polynomial fit to the two standard gas measurements

533   stated above.

534   In the first period of the measurement when both analyzers measured dried ambient

535   air, the absolute differences between the 1-minute averages measured over two days by the

536   two analyzers were mostly within 15 ppm (Figure 15c) and symmetrically distributed around

537   zero (Figure 15e). However, when wet air was admitted to the CRDS analyzer and the in-built

538   water correction was applied, a stronger variability was observed in the calculated differences

539   (Figure 15d). This implies stronger short term variability in the CRDS analyzer measurement

540   values (as nothing was changed for the Paramagnetic measurement system) when wet samples

541   were analyzed. The more negative values in the differences (Figure 15f) can also be

542   associated with overestimation of the O_2 mixing ratios by the CRDS originating from an

543   overestimated water correction. However, detailed evaluation of the analyzer's water

544   correction function is beyond the scope of this study.

545   **3.3. Field Measurements**

546   After a series of tests at University of Bern, we conducted multiple field measurements

547   at the High Altitude Research Station Jungfraujoch and the Beromünster tall tower sites in

548   Switzerland described below.

549   3.3.1. Tests at the High Altitude Research station Jungfraujoch

550   The High Alpine research station Jungfraujoch is located on the northern ridge of the

551   Swiss Alps (46° 33′ N, 7° 59′ E) at an elevation of 3580 m a.s.l. It is one of the global

552   atmospheric watch (GAW) stations well-equipped for measurements of numerous species and

553   aerosols. The site is above the planetary boundary layer most of the time due to its high

554   elevation (Henne et al., 2010; Zellweger et al., 2003). However, thermally uplifted air from

555   the surrounding valleys during hot summer days or polluted air from the heavily industrialized

556   northern Italy may reach at this site (Zellweger et al., 2003). The Division of Climate and

557   Environmental Physics at the University of Bern has been monitoring CO_2 and O_2 mixing

558   ratios at this site based on weekly flask sampling and continuous measurements since 2000

559   and 2004, respectively (Schibig et al., 2015). The CO_2 mixing ratio is measured using a

560   commercial NDIR analyzer (S710 UNOR, SICK MAIHAK) while O_2 is measured using the

561   Paramagnetic sensor (PM1155 oxygen transducer, Servomex Ltd, UK) and fuel cells (Max-

562   250, Maxtec, USA) installed inside a home-built controlling unit. Similar to the comparison

563   tests at the University of Bern, we have conducted parallel measurements between the CRDS

564   analyzer and the paramagnetic cell at this high altitude site during 03 – 14 February 2017. The

565   measurement of ambient air at the Jungfraujoch system is composed of sequential switching

566   between low span (LS) and high span (HS) calibration gases followed by a target gas (T)

567   measurement (once a day) to evaluate the overall system performance and finally a working

568   gas (WG) measurement before switching back to ambient air.

Figure 16 (top panel) shows the calibrated 1-minute averaged O_2 mixing ratios measured at this high altitude site in comparison with the Paramagnetic oxygen analyzer already available at the site. Despite the strong variability observed during the measurement period of 10-days by both analyzers, a very good agreement was observed between them.

Figure 16 (bottom panel) shows the absolute difference of 1-minute averages in atmospheric O_2 measured at Jungfraujoch between the two analyzers which are mostly within ± 5 ppm range (but sometimes going as high as ± 10 ppm) without an offset. However, for generally reported 10-minutes, half-hourly or hourly means these values correspond to < 1.5 ppm, < 1 ppm and < 0.65 ppm.

3.3.2. Tests at the Beromünster tall tower site

The Beromünster tower is located near the southern border of the Swiss Plateau, the comparatively flat part of Switzerland between the Alps in the south and the Jura mountains in the northwest (47° 11′ 23″ N, 8° 10' 32″ E, 797 m a.s.l.), which is characterized by intense agriculture and rather high population density. A detailed description of the tower measurement system as well as a characterization of the site with respect to local meteorological conditions, seasonal and diurnal variations of greenhouse gases, and regional representativeness can be obtained from previous publications (Berhanu et al., 2016; Berhanu et al., 2017; Oney et al., 2015; Satar et al., 2016). The tower is 217.5 m tall with access to five sampling heights (12.5 m, 44.6 m, 71.5 m, 131.6 m, 212.5 m) for measuring CO, CO_2, CH_4 and H_2O using Cavity Ring Down Spectroscopy (Picarro Inc., G-2401). By sequentially switching from the highest to the lowest level, mixing ratios of these trace gases were recorded continuously for three minutes per height, but only the last 60 seconds were retained for data analysis. The calibration procedure for ambient air includes measurements of reference gases with high and low mixing ratios traceable to international standards (WMO-

593   X2007 for CO_2 and WMO-X2004 for CO and CH_4), as well as target gas and more frequent

594   working gas determinations to ensure the quality of the measurement system. From two years

595   of data a long-term reproducibility of 2.79 ppb, 0.05 ppm, and 0.29 ppb for CO, CO_2 and

596   CH_4, respectively was determined for this system (Berhanu et al., 2016).

597   Between 15.02.2017 and 02.03.2017, we have connected the new CRDS oxygen

598   analyzer in series with the CO_2 analyzer (Picarro G-2401) and measured the O_2 mixing ratios

599   at the corresponding heights. Similar to the CO_2 measurements, O_2 was also measured for

600   three minutes at each height. During this period, we have evaluated the two features (isotopic

601   mode and concentration mode) of the CRDS analyzer. In the isotopic mode, the CRDS

602   measures the $\delta^{18}O$ values as well as the O_2 concentration while in concentration mode only

603   the latter was measured.

604   During the tests conducted at this tower site, we first evaluated the two operational

605   modes (concentration vs isotopic modes) of the CRDS analyzer. Ambient air measurements

606   on isotopic mode over a 4-days period showed a strong variability in the measured oxygen

607   mixing ratios and it was not possible to distinguish the variability in the O_2 mixing ratios

608   among the five height levels. The calculated 1-minute standard error for ambient air

609   measurements was as high as 10 ppm while a standard error of less than 1 ppm was

610   determined from similar measurements in the concentration mode. Additionally, comparing

611   the O_2 values between the two modes, frequent short time variation in ambient air O_2 (~ 200

612   ppm) was observed in the isotope mode measurements while the variation in the concentration

613   mode is significantly smaller (~ 30 ppm). This precision degradation is due to the weaker ^{16}O

614   oxygen line used for the isotopic mode, and the fact that far more ring-downs are collected on

615   the rare isotopologue in isotopic mode Hence, we have conducted the remaining test

616   measurements in concentration mode.

As this tower has five sampling height levels, we first followed three minutes of switching per inlet level, which enables four measurements per hour at a given level. However, we noticed hardly any difference among the different levels due to strong short term variability in O_2 mixing ratios between the consecutive heights. Hence, we switched to a longer sampling period of six-minutes per height. Figure 17 shows the diurnal CO_2 and O_2 variations at the lowest (12 m) and highest (212.5 m) sampling heights of the tower. These two heights were selected simply to better illustrate the difference in the mixing ratios. The CO_2 mixing ratios on the top panel show higher values at the 12 m inlet than the highest level most of the day due to its closeness to sources except during the afternoon (11:00 - 17:00 UTC) when both levels show similar but decreasing CO_2 mixing ratios. This is due to presence of a well-mixed planetary boundary layer (PBL) (Satar et al., 2016). The lag in CO_2 peak between the two height levels by about two hours indicates the duration for uniform vertical mixing along the tower during winter 2017. The opposite variability patterns are also clearly visible in the O_2 mixing ratios shown in the lower panel with a clear distinction between the two height levels during early in the morning and in the evening while similar O_2 values were observed in the afternoon. These opposing profiles are expected as CO_2 and O_2 are linearly coupled with a mean oxidation ratio of -1.1 ± 0.05 (Severinghaus, 1995) for land-biospheric processes (photosynthesis and respiration) and -1.44 ± 0.03 for fossil fuel burning (Keeling, 1988b).

Table 2 shows the oxidation ratios derived as the slopes of the linear regression between CO_2 and O_2 mixing ratios at the different height levels measured on 25 February 2017. Accordingly, height dependent slopes were observed with a slope of -0.98 ± 0.06 at the lowest level, close to the biological processes induced slope but slightly lower than its mean value. For the highest level, we calculated a slope of -1.60 ± 0.07 a value close to fossil fuel

combustion oxidation ratio. Note that depending on fossil fuel type the oxidation ratio can range between -1.17 and -1.95 for coal and natural gas, respectively (Keeling, 1988b). While the slopes derived for the two other levels (44.6 m and 131.6 m) show similar values between the highest and lowest height levels, possibly from mixed sources, the middle level showed a slightly higher slope than these two levels but still in the large range between the lowest and highest inlet heights.

3.4. Evaluation of the $\delta^{18}O$ measurements

To further evaluate the analyzer's performance in measuring stable oxygen isotopes, we conducted ambient air isotopic composition measurements as well as analyzed a standard gas without CO_2 which has a known $\delta^{18}O$ value. The choice of this CO_2-free air standard gas is twofold: one it has a known $\delta^{18}O$ value and second as it has no interference from possible CO_2 absorption band overlap. For this test three 0.5 L glass flasks were preconditioned and filled with this standard gas to ambient pressure. These flasks were attached before or after the water trap (Fig. 11) and measured similar to ambient air measurements. These measurements were then compared with $\delta(^{34}O/^{32}O)$ values obtained by parallel measurements using our IRMS.

Figure 18 shows the $\delta^{18}O$ values of ambient air from the roof top with three consecutive measurements of glass flasks filled with CO_2-free air in-between followed by a fourth flask filled with breath air. An excellent agreement was observed for measurements from both instruments for the three flasks filled with a standard gas. However, the fourth flask with breath air showed a signal opposite to the measurements by the IRMS. As breath air contains large amount of water and CO_2 in addition to O_2, which can possibly interfere with the CRDS analyzer measurements, we have removed H_2O and CO_2 by using a cryogenic trap (-130 °C) and in an additional experiment using Schütze reagent to remove both CO and CO_2.

665 However, we have not observed any improvement towards an agreement with the IRMS

666 measurements. Therefore, any other gas component in the breath air must be relevant for the

667 interference. Based on the absorption lines in the spectral range of the instrument (7878 cm^{-1})

668 retrieved from HITRAN database, we expect interference either from carbon monoxide (now

669 excluded by the tests) or methane or VOCs including acetone, ethanol, methanol or isoprenes,

670 all of which have been measured in breath air (Gao et al., 2017; Gottlieb et al., 2017; Mckay

671 et al., 1985; Ryter and Choi, 2013; Wolf et al., 2017). Further investigations have to shed light

672 on these interferences in order to take corresponding action to surpass these shortcomings in

673 the isotope analysis based on cavity ring-down spectroscopy.

674 **4. Conclusions**

675 We have thoroughly evaluated the performance of a new CRDS analyzer which

676 measures O_2 mixing ratios and isotopic composition combining laboratory and field tests.

677 Even if a drift in the analyzer was observed at the beginning of this study, which can be easily

678 corrected by calibration, the recent analyzers built by the manufacturer did not show such

679 instrumental drift. However, prior tests are recommended to see the analyzer's stability.

680 The T-split tests for the current measurement setup based on the measurements of two

681 standard gases showed a difference within the measurement uncertainty. However, this effect

682 may become significant while applying larger splitting ratios and we recommend conducting

683 further experiments to accurately quantify this influence for larger splitting ratios.

684 We have observed a strong influence of dilution in the measured O_2 values during the

685 presence of high CO_2 mixing ratios. Even if such an influence may not be critical for the

686 present study, such an effect might be significant in other studies where higher CO_2 mixing

687 ratios might be present and we recommend following a correction strategy based on parallel

688 CO_2 measurements. This also applies for more accurate analysis.

The water correction applied by the instrument's in-built function seems to sufficiently correct for the water vapor influence. However, a larger variability of the difference was observed between the CRDS analyzer and the Paramagnetic cell when dried samples were used in both systems. This can possibly be due to an overcorrection by the water correction function of the CRDS analyzer when dried samples were used. This is particularly true for the very low water vapor range (< 100 ppm). We believe that it is important to further investigate this issue and identify an improved water correction strategy.

Based on the analysis of O_2 mixing ratios in the concentration and isotopic modes, we have observed a significant decrease in precision (about ten-fold) in the latter measurement mode. The measured $\delta^{18}O$ values for the standard air by the CRDS analyzer are in excellent agreement with the IRMS values. However, such measurements for a breath air showed a contrasting signal, possibly due to interference from other gases such as CH_4. Hence, we recommend further investigation on such possible contaminants and how to possibly remove them while conducting ambient air measurements. However, we believe that this analyzer can be used for tracer experiments where artificially enriched isotopes are used to study biological processes such as photosynthesis in plants using isotopically labelled CO_2 and H_2O.

Acknowledgement

We would like to thank ICOS-RI and the Swiss National Science Foundation (SNF) for funding ICOS-CH (20FI21_148994, 20FI21_148992). We are also grateful to the International Foundation High Alpine Research Stations Jungfraujoch and Gornergrat. The measurement system at the Beromünster tower was built and maintained by the CarboCount-CH (CRSII2_136273) and IsoCEP (200020_172550) projects both funded by SNF.

713

714

715

716

717

718

719

720   List of Tables

721   Table 1. Assigned mixing ratios of standard gases used in this study and their corresponding

722   values measured by the NDIR, CRDS and IRMS at the University of Bern. [1]The assigned

723   values are based on measurements from different institutions (University of Bern (UB),

724   Scripps or NOAA, see column cylinder name). [2]Measurements are on the Bern scale for CO_2

725   and O_2. The Bern scale is shifted by +550 per meg. [3]Values on the Scripps scale.

726

Cylinder name	Assigned CO_2 (ppm) [1]	Assigned O_2 (per meg) [1]	CO_2-IRMS (ppm) [2]	CO_2-NDIR (ppm) [2]	O_2-IRMS (per meg) [2]	O_2-Paramagnetic (per meg) [2]	O_2-CRDS (per meg) [2]
ST-1 LUX3576-UB	427.47	-1026	427.47	427.59	-1026	-1070	-1057
ST-2 LK922131-UB	368.09	599	368.09	367.82	599	560	590
ST-3 CA07045-Scripps	382.303	-271.6	382.50	381.99	278 (-272.2)[3]	302	281

ST-4 CA07043-Scripps	390.528	-476.4	390.69	390.15	71 (-479.5)[3]	66	63
ST-5 CA07047-Scripps	374.480	-807.7	374.70	374.17	-253 (-803.3)[3]	-212	-233
ST-6 CA04556-NOAA	192.44	-3410	191.21	191.64	-3410	-2905	-3013
ST-7 CA06943-NOAA	2699.45	-		2612.80	-	-2691	-3369
ST-8 LK76852-UB	411.49	37794	411.49	406.25	37794	34513	36017

727

728

729 Table 2. The CO_2 and O_2 correlation coefficients at the different height levels derived using

730 the least square fit and the correlation coefficients (r^2). Uncertainties are calculated as

731 standard error of the slope.

Height	Oxidation Ratios (O_2:CO_2)
12.5 m	-0.98 ± 0.06 (0.48)
44.6 m	-1.29 ± 0.07 (0.50)
71.5 m	-1.49 ± 0.08 (0.47)
131.6 m	-1.23 ± 0.05 (0.55)
212.5 m	-1.60 ± 0.07 (0.61)

732

733

734

735

736

737

738

739

740   List of Figures
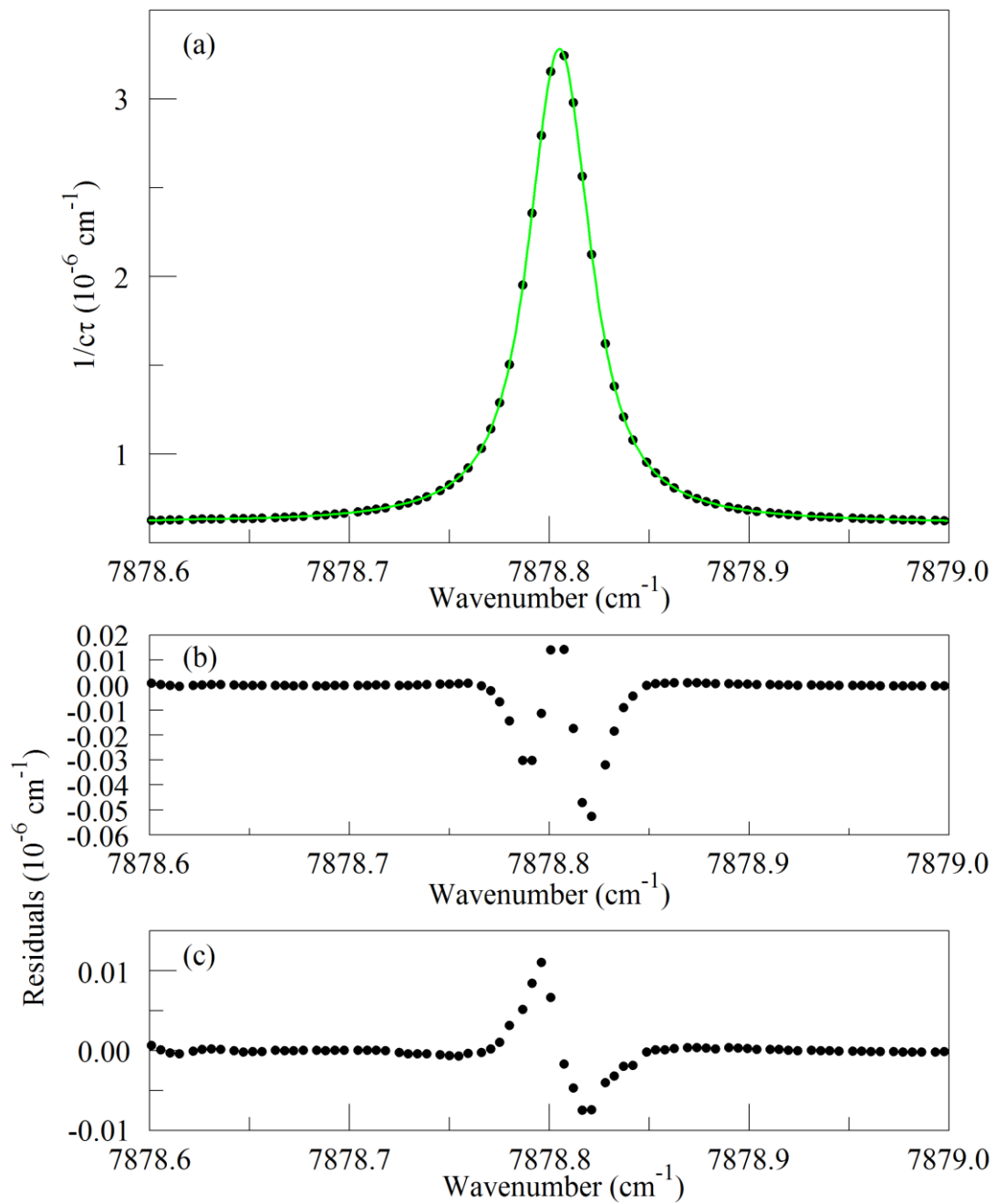
741

742   Figure 1. The top panel (a) shows the raw data (points) and the best-fit Galatry function (solid

743   line). Residuals of the Voigt fit are shown in panel (b) and residuals of the Galatry fit are

744   shown in panel (c).

745

746
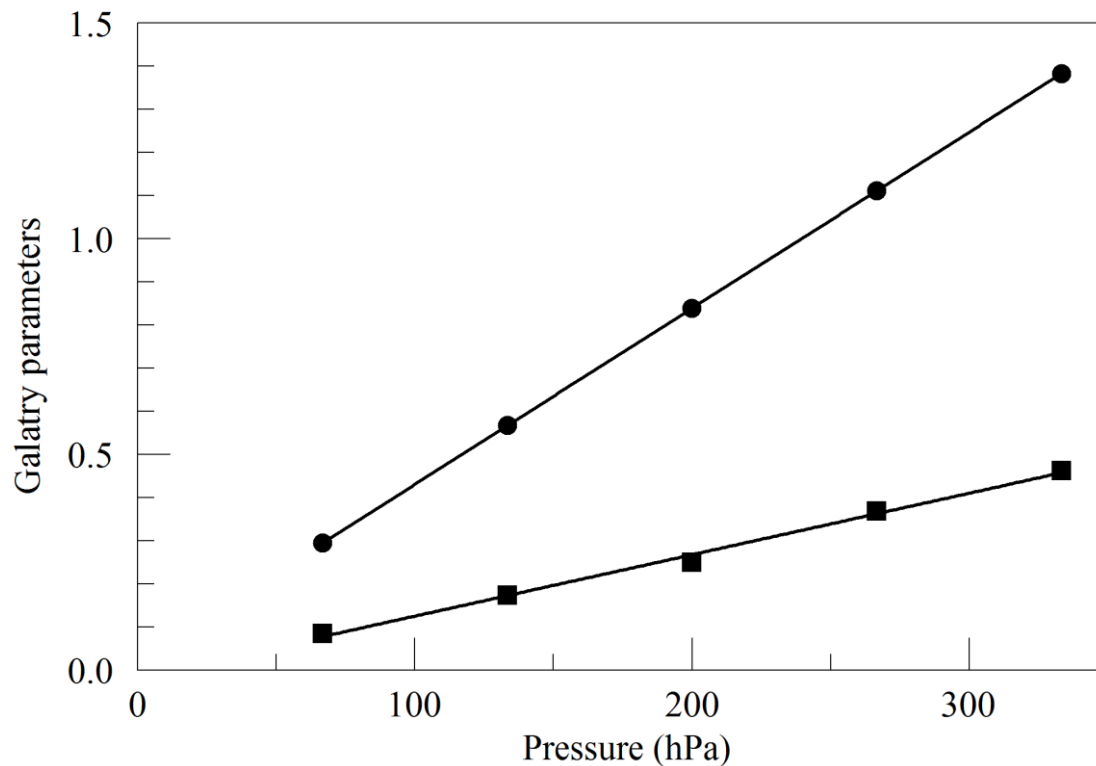
747

748 Figure 2. Best-fit values for the Galatry parameters of the Q13Q13 line of O_2, as a function of

749 pressure. The line broadening parameter y is represented by circles and the line narrowing

750 parameter z by squares. The solid lines are linear fits to the measurements. The best-fit offset

751 and slope are 0.0227 and 0.004082 hPa^{-1} for y, and -0.0169 and 0.001424 hPa^{-1} for z.
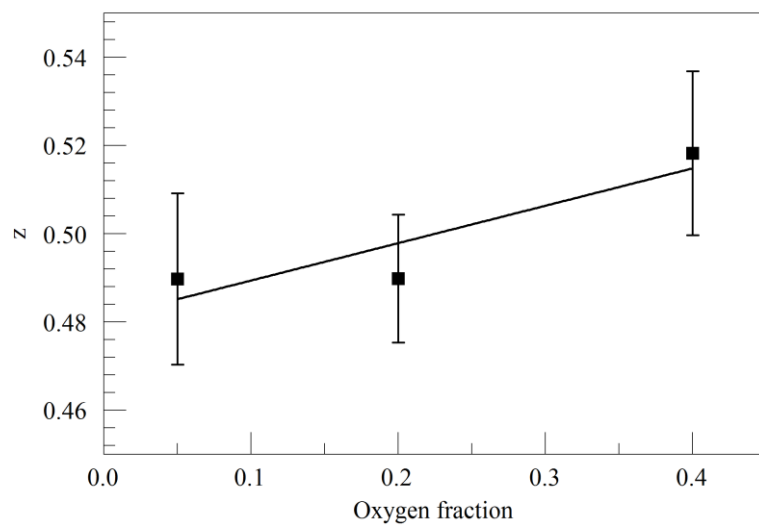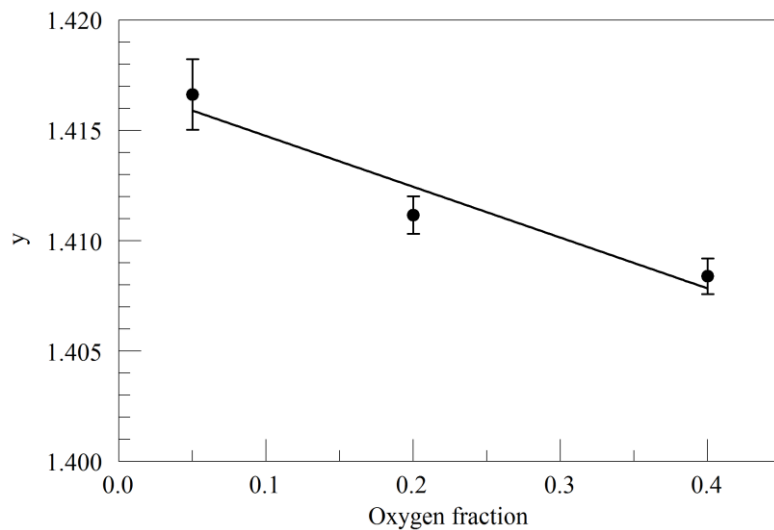
752

753   Figure 3. Galatry parameters of the Q13Q13 line of O_2 at 340 hPa and 45° C as a function of

754   O_2 mole fraction in binary O_2 - N_2 mixtures. The linear fits to the data are y = 1.417 – 0.023 x

755   f_{O2} and z = 0.481 + 0.085 x f_{O2}.
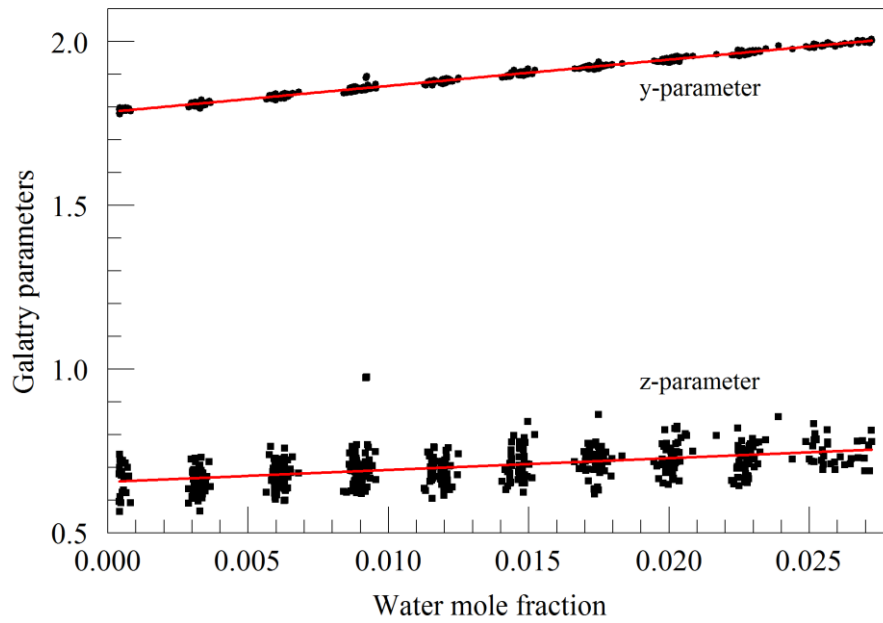
756

757 Figure 4. Galatry parameters of the 7816.75210 cm^{-1} water line in air at 340 hPa and 45° C as

758 a function of water mole fraction. Black points are from measurements and red lines are

759 linear fits: $y = 1.7846 + 8.01 \times f_{H2O}$ and $z = 0.656 + 3.60 \times f_{H2O}$.

760

761

762
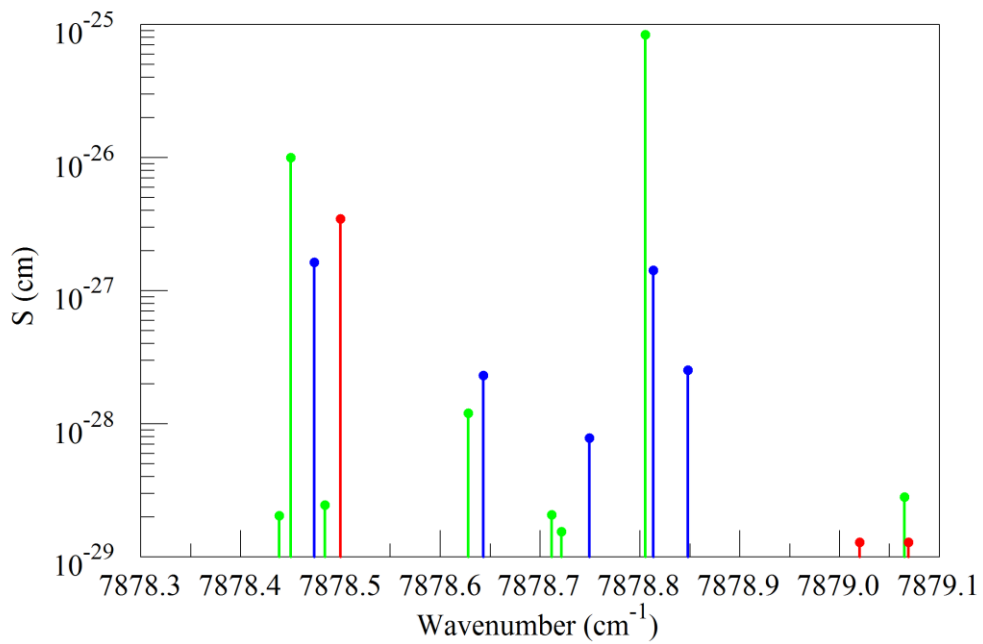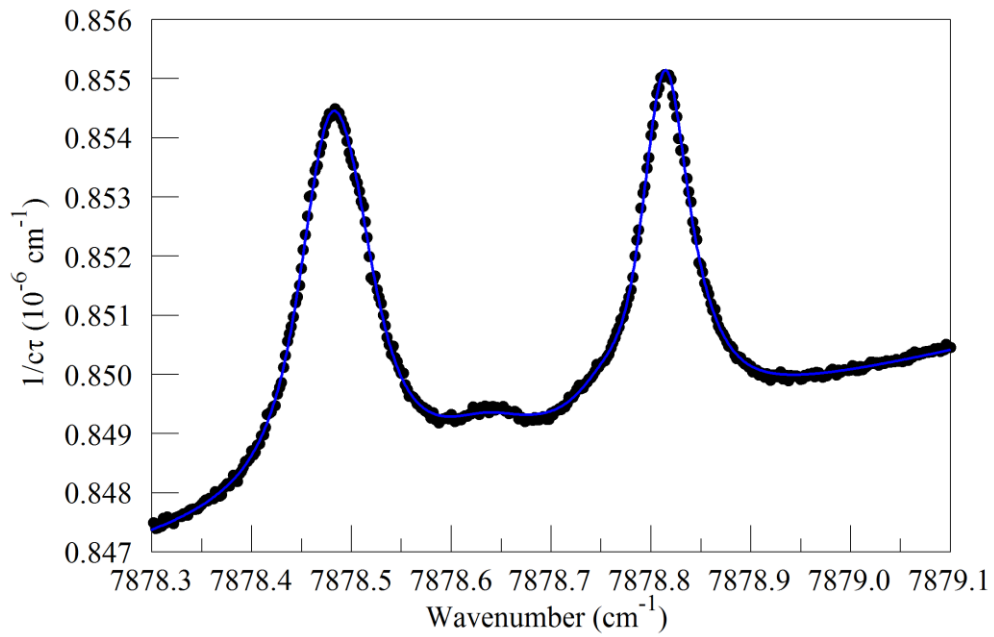
763

764 Figure 5. Upper panel: spectrum of water in nitrogen (points) and fit to Voigt model (blue

765 curve). Lower panel: Oxygen (green), normal water (blue), and deuterated water (red) lines

766 in the 2016 Hitran data base.

767

768
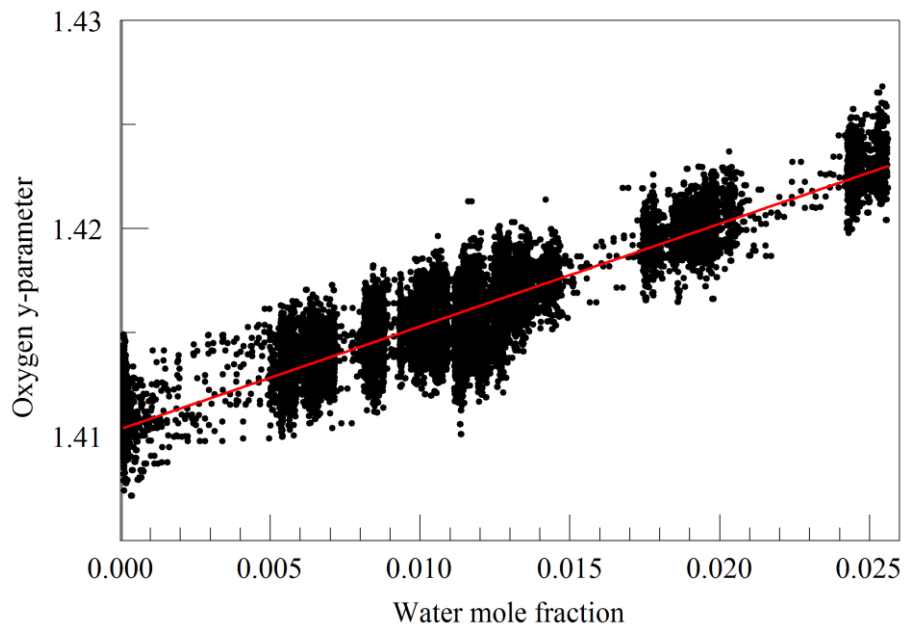
769

770   Figure 6. Galatry collisional broadening parameter of the oxygen Q13Q13 line at 340 hPa

771   and 45° C versus water mole fraction. Black points are from measurements and the red line is

772   a linear fit: $y = 1.4109 + 0.467\, f_{H2O}$.

773

774

775
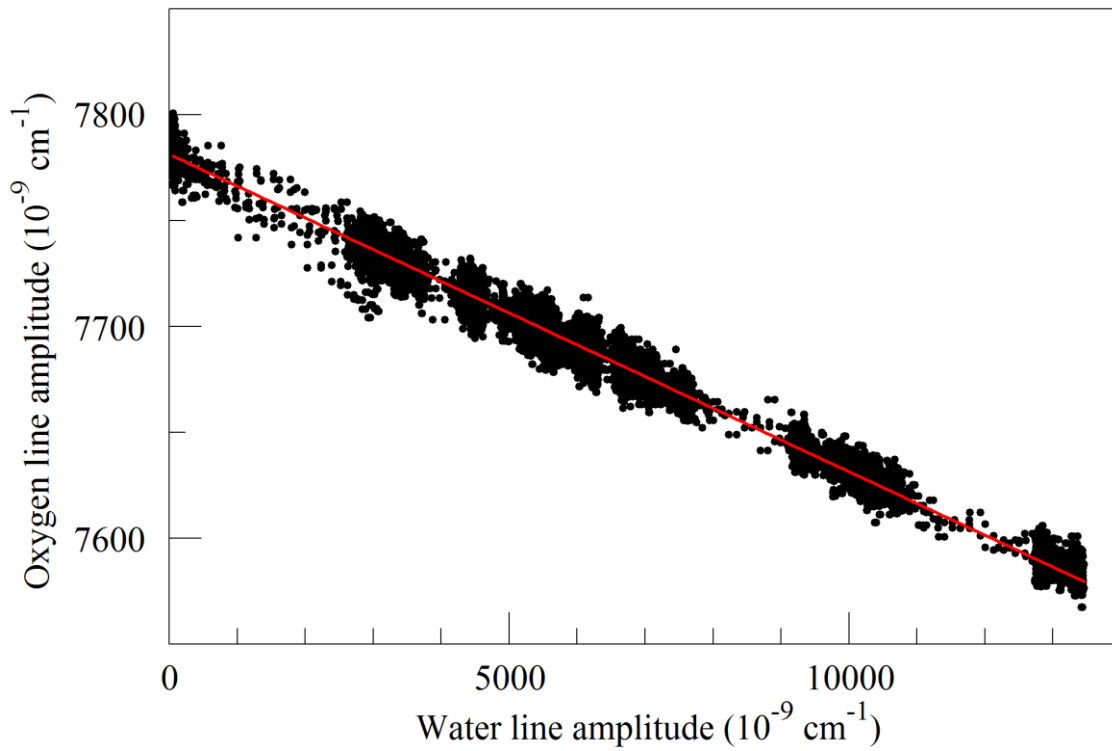
776

777   Figure 7. Measured absorption line amplitudes for oxygen and water vapor for water vapor

778   mixing ratios ranging from nearly 0 to 0.025. Black points are from measurements and the

779   red line is a linear fit: with intercept 7.78001×10^{-6} cm^{-1} and slope -0.014807.

780

781

782

783

784

785

786
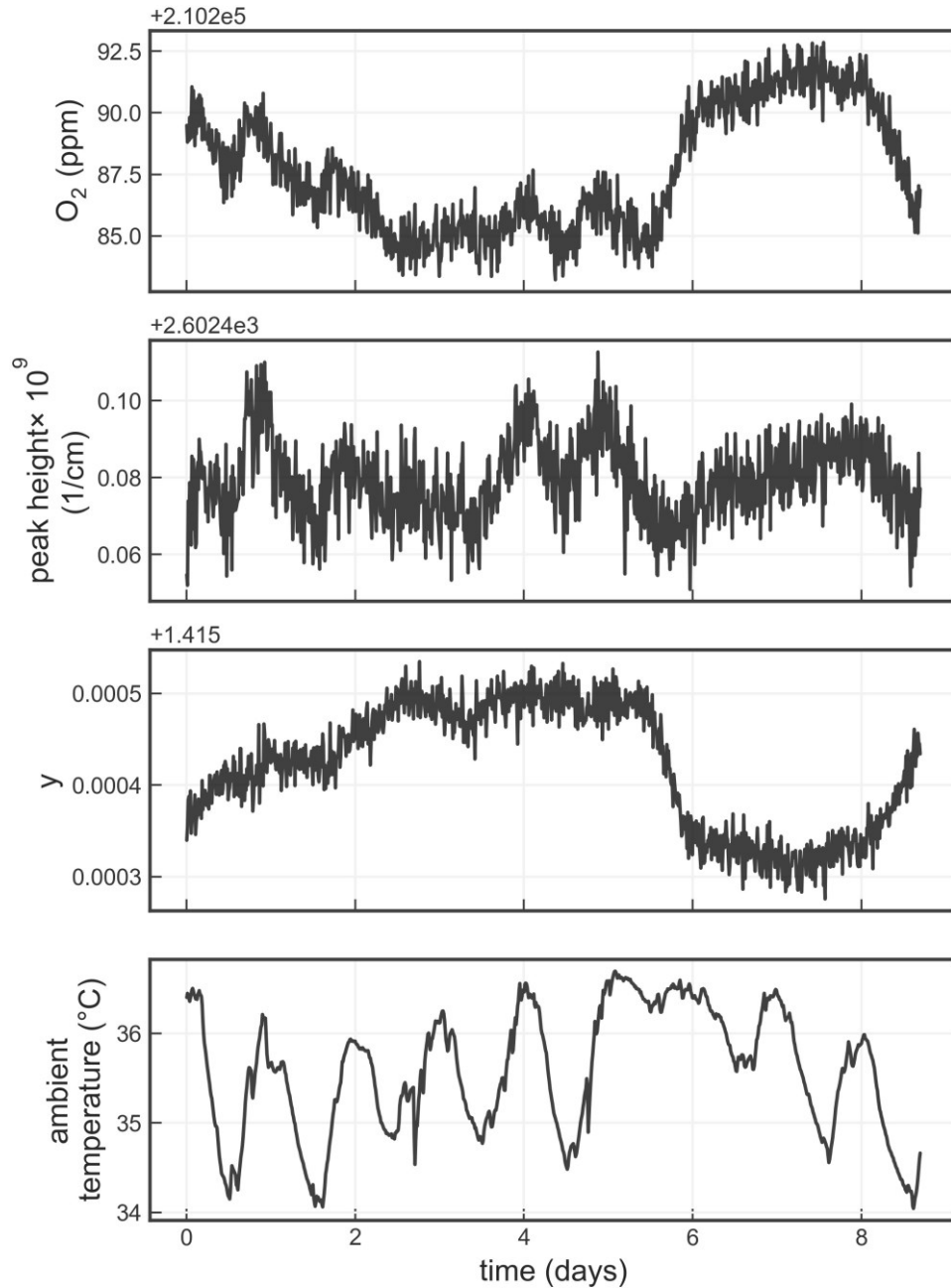
Figure 8. Time series from a measurement of a single tank over about a week. The four panels

show the water-corrected oxygen concentration, the absorption peak loss minus the baseline

loss, the measured Lorentzian broadening factor, and the ambient temperature (measured in

the instrument housing), respectively. A windowed average of 300 seconds was applied to all

four data sets.
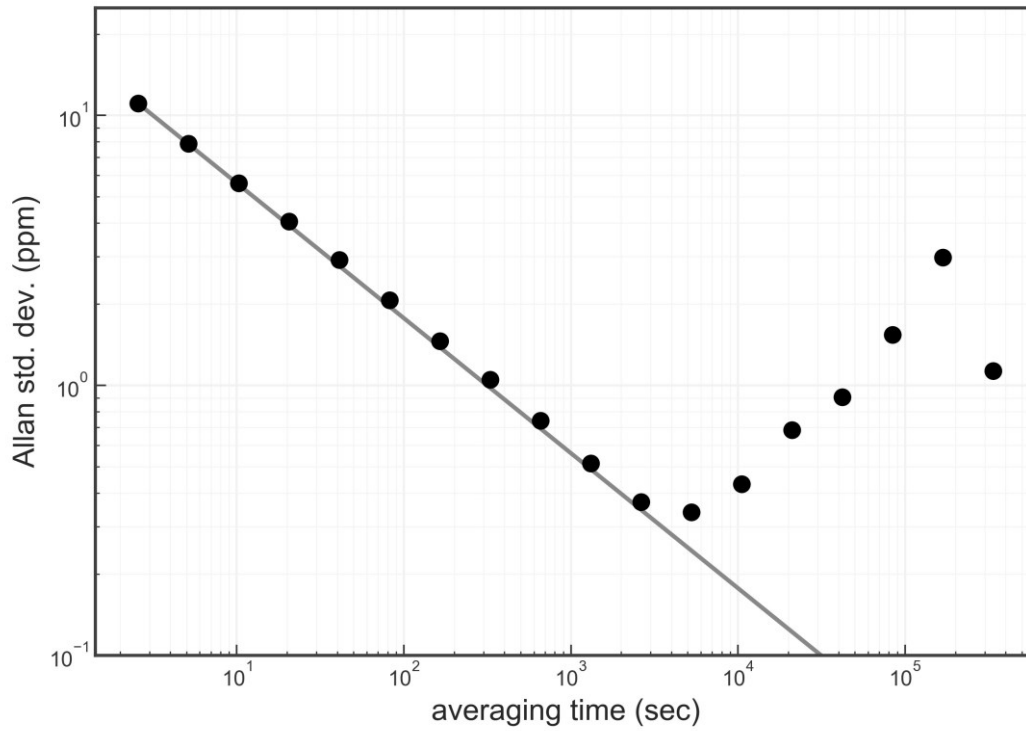
792

793   Figure 9. Precision of O_2 mole fraction measured from a tank of synthetic air. Filled circles

794   are measurements and the line shows the ideal $\tau^{-1/2}$ dependence.

795

796

797

798

799

800

801   Figure 10. Precision of $\delta(^{18}O)$ measured from a tank of synthetic air. Filled circles are

802   measurements and the line shows the ideal $\tau^{-1/2}$ dependence.

803

804

805

806

807

808

809

810
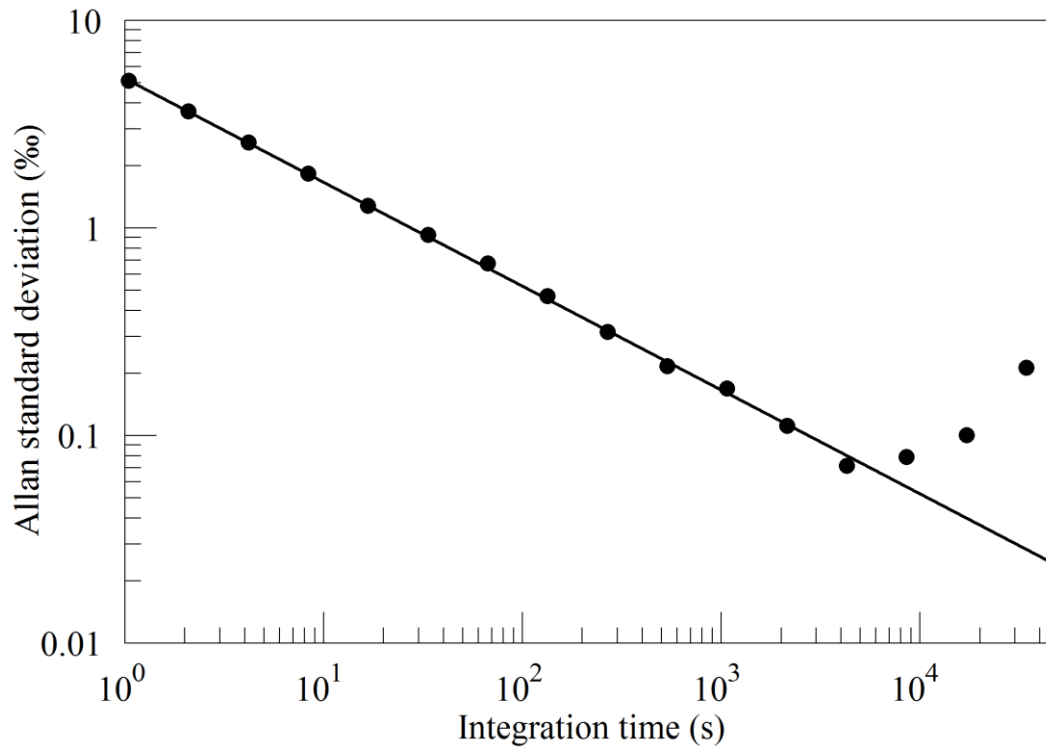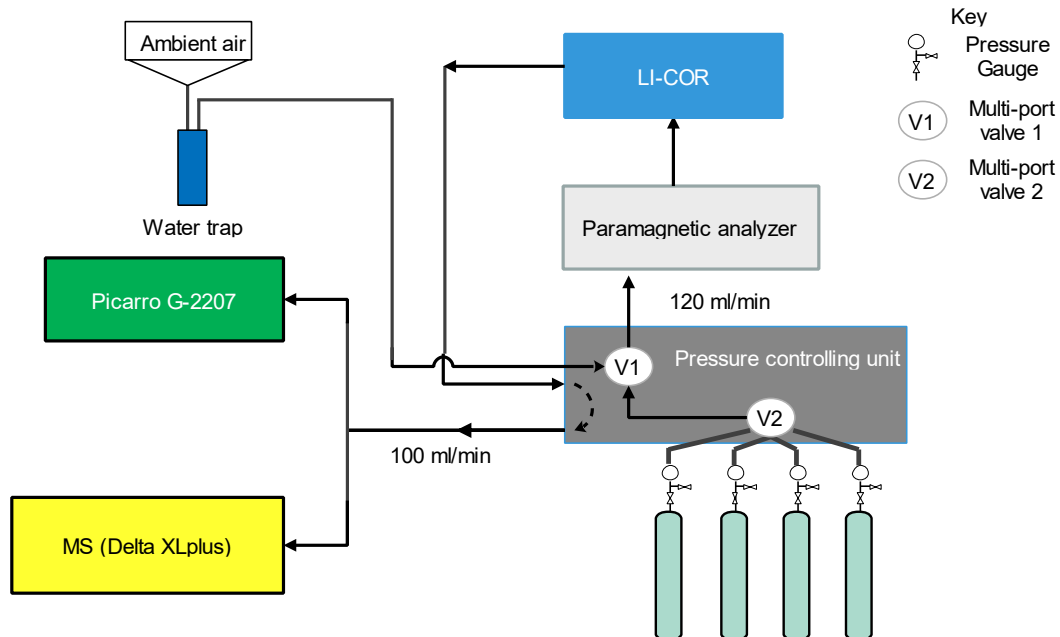
811

812 Figure 11. Schematics of the measurement system used to compare the Picarro analyzer with

813 the Mass Spectrometer at Bern.

814

815

816

817

818

819

820

821

822
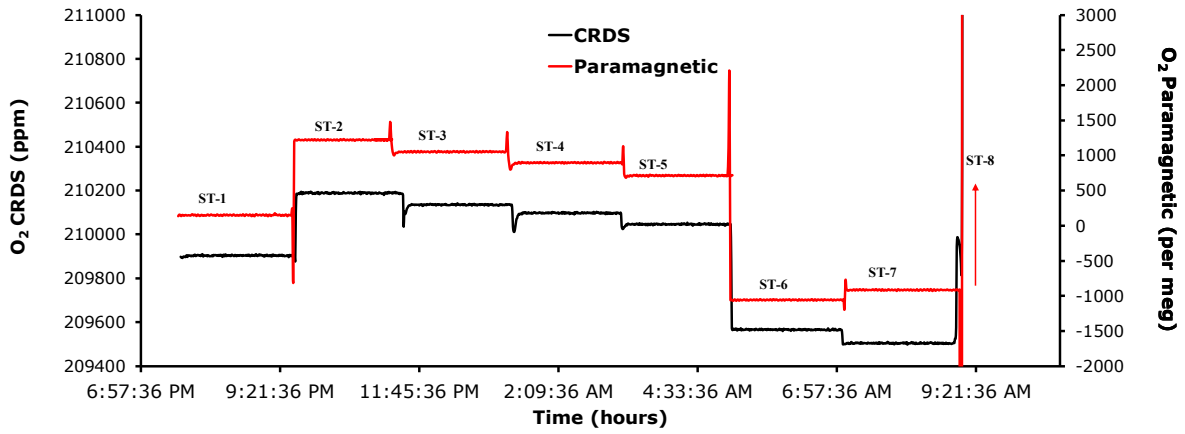
823

824 Figure 12. Comparison of oxygen mixing ratios for the seven standard gases measured using

825 the CRDS analyzer (black) and the Paramagnetic sensors (red).

826

827

828

829

830

831

832

833

834

835

836

837

838

839

840

841

842
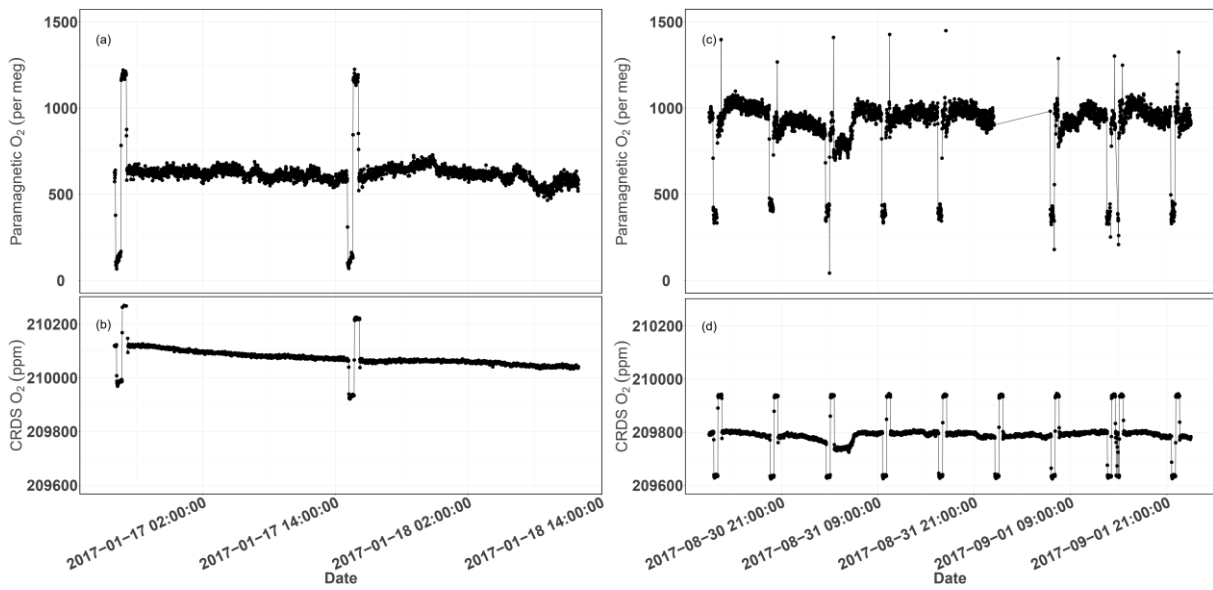
Figure 13. Parallel ambient air measurements by the Paramagnetic and CRDS analyzers at the

beginning of the testing period (Panels a & b, January 2017) and the second phase of testing

(Panels c & d, September 2017). The spikes are measurements from the two standard gases

bracketing the ambient air values.

847

848

849

850

851

852

853

854

855

856

857

858
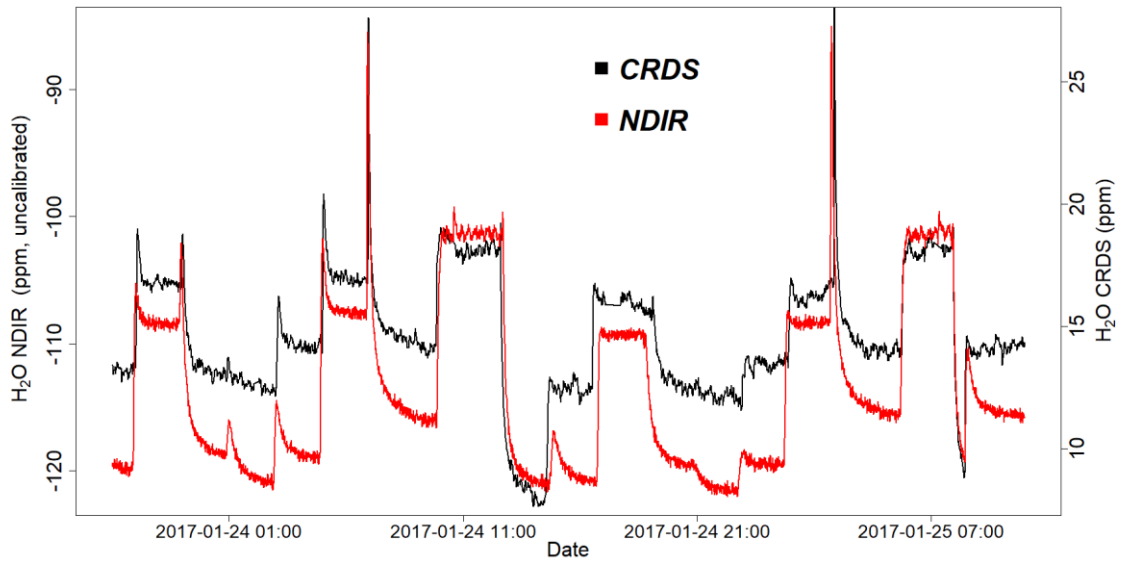
859

860 Figure 14. Parallel water vapor measurements for a dried ambient air by both the NDIR and

861 CRDS analyzers. Note that the water values from the NDIR analyzer are not calibrated.

862

863

864

865

866

867

868

869

870

871

872

873

874

875

876
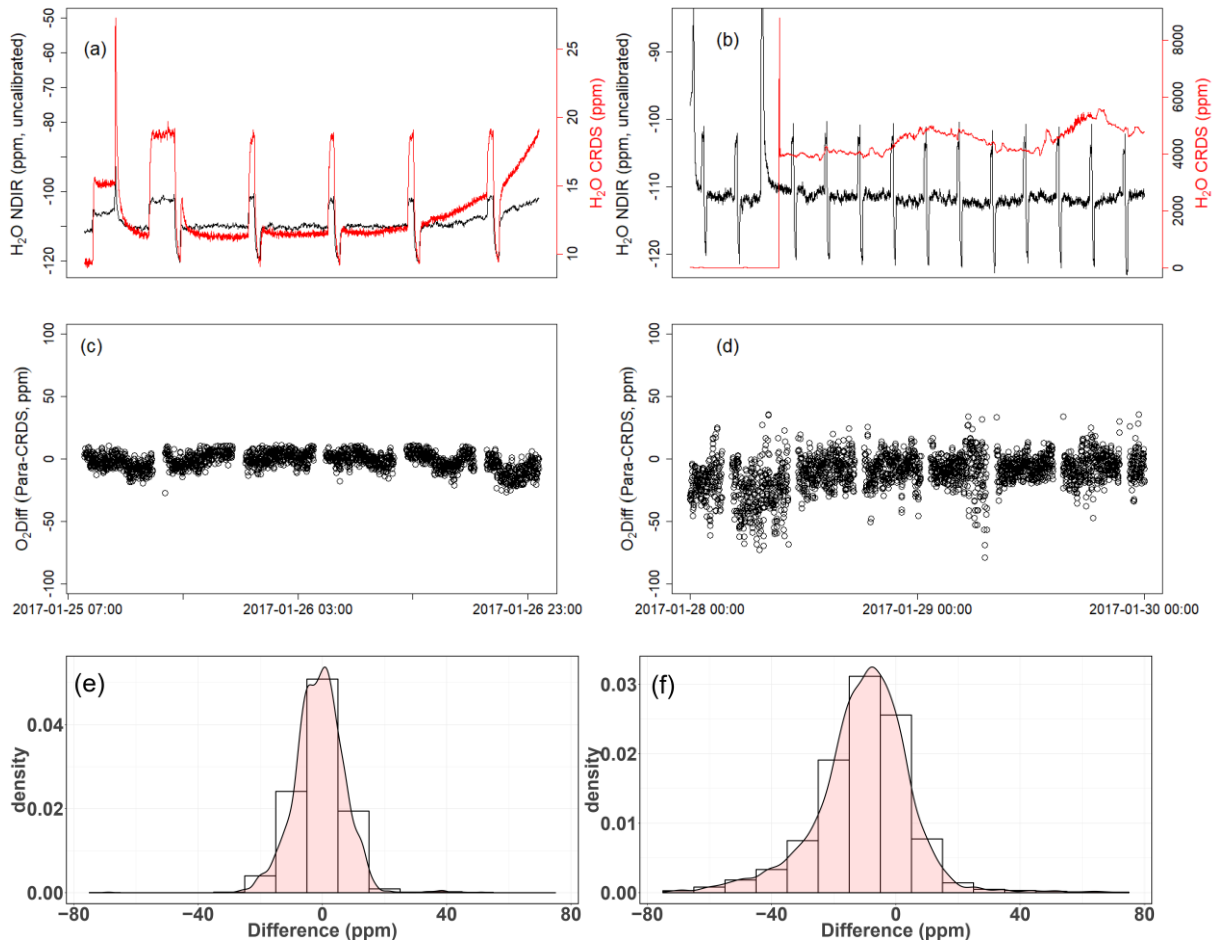
Figure 15. Results of water correction tests. Water measurements of the NDIR (left scale) for

dry conditions (a,b) and the CRDS analyzer (right scale) for dry (a) and wet (b) conditions.

The difference in oxygen measurements between the Paramagnetic and the CRDS instrument

using the built-in water correction for the CRDS values under dry (c) and wet (d) conditions.

Panels (e) and (f) show the population density functions.

882

883

884

885

886

887

888
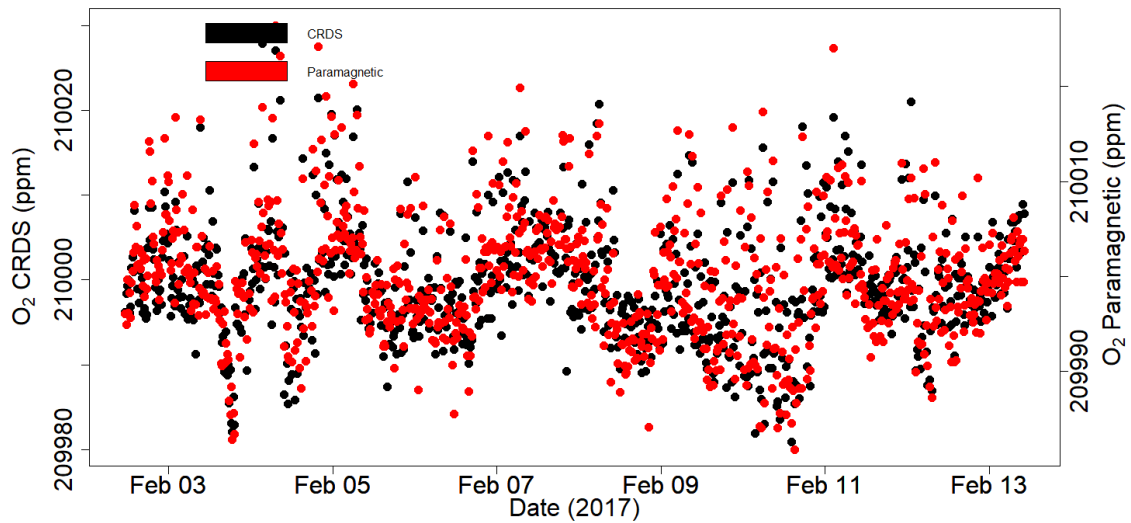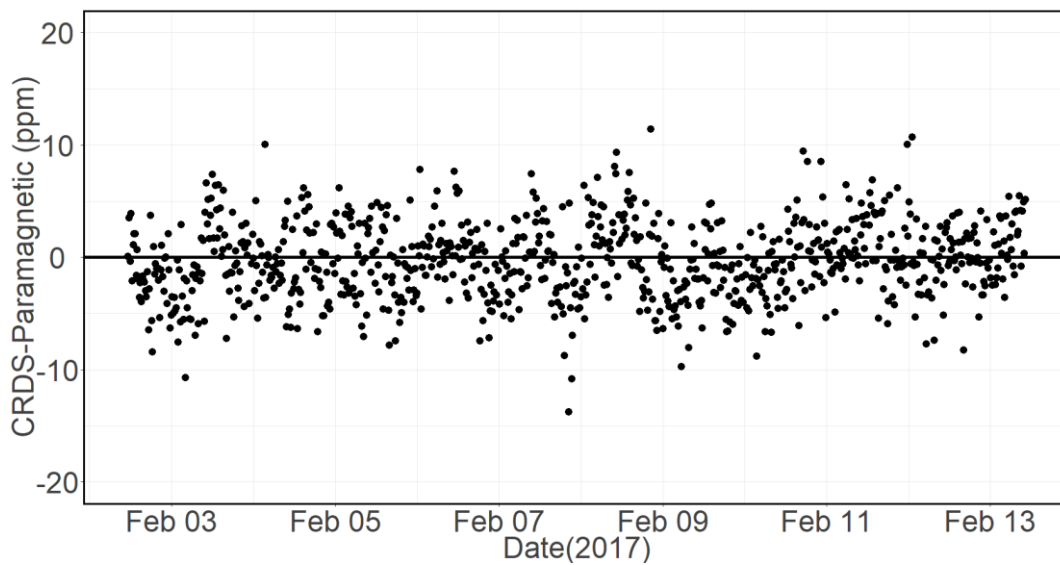
Figure 16. Calibrated ambient air oxygen measurements (1-minute average) at the Jungfraujoch site using the CRDS and Paramagnetic analyzers both in ppm units (a) and the absolute difference between the two measurements in ppm (b) by matching time stamps

892

893

894

895

896
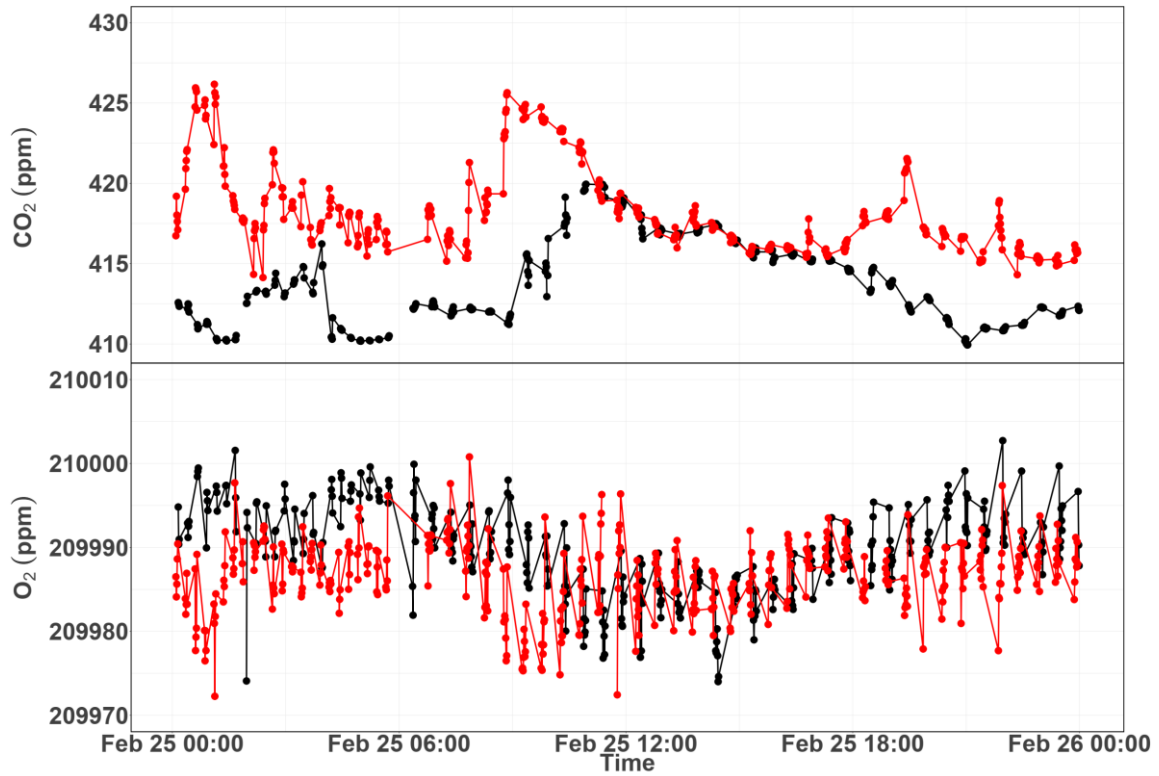
897

898 Figure 17. Diurnal variations of CO_2 (top) and O_2 (bottom) measurements from the 12 m (red)

899 and the 212.5 m (black) height levels at Beromünster tower.

900

901

902

903

904

905

906

907

908

909
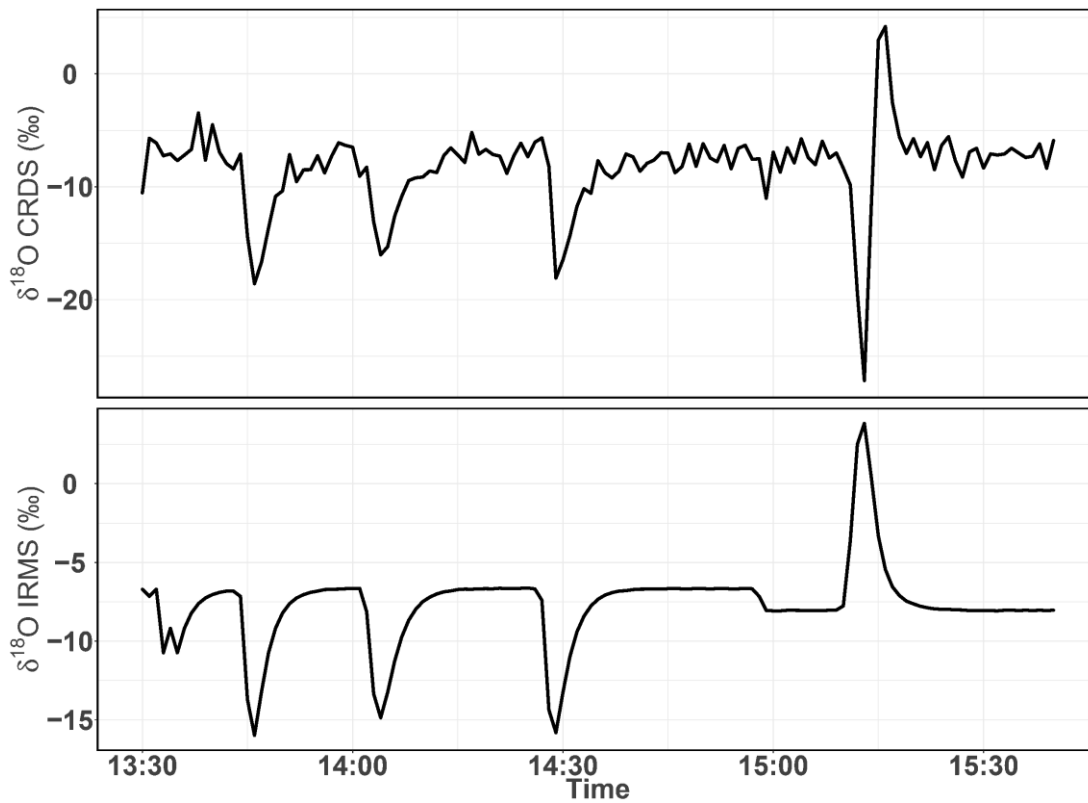
Figure 18. Consecutive $\delta^{18}O$ measurements of a standard gas (CO_2-free air) filled into three flasks followed by measurement of breath air using the CRDS analyzer (top) and IRMS (bottom). These measurements were carried out in the middle of ambient air measurements.

924   **Appendix A.**

925
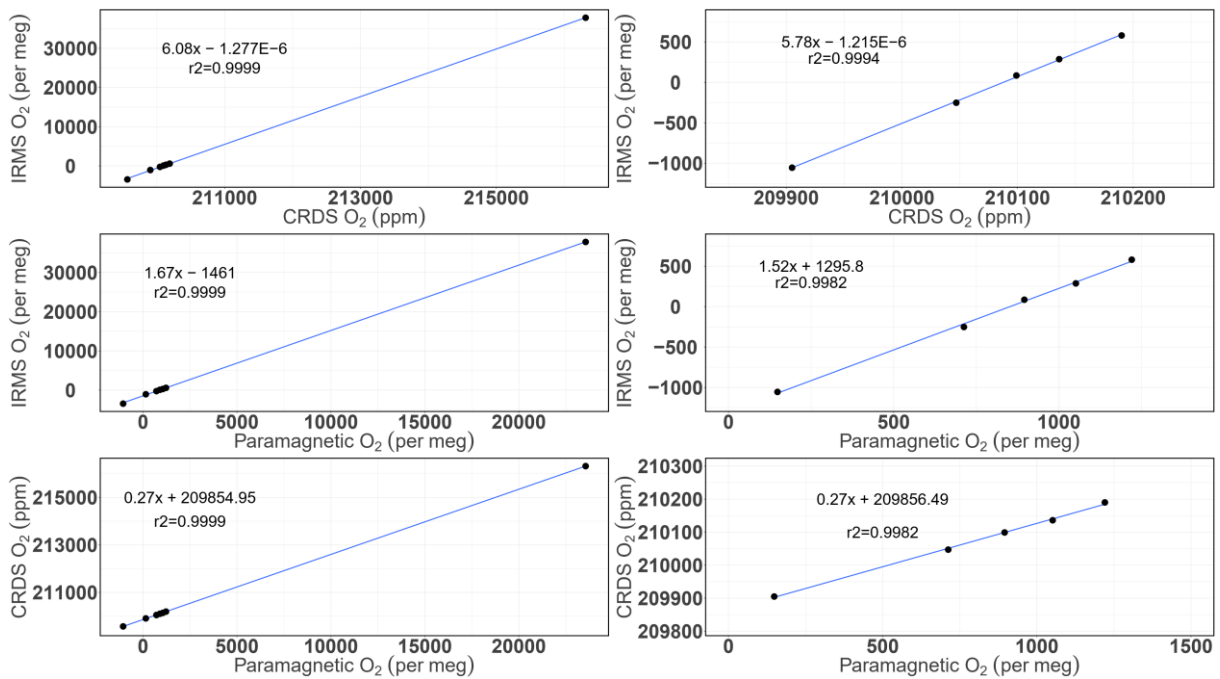
927   Figure A.1. Correlations between the O_2 mixing ratios measured by the CRDS and

928   Paramagnetic analyzers with the mass spectrometric measurements (uncalibrated values). The

929   left panels are for all the cylinders measured (standards 1 to 8) while the right ones are after

930   selecting standards 1-5.

931

932

933

934

935

936

937

938

References

939 **References**

940 Battle, M., Bender, M. L., Tans, P. P., White, J. W. C., Ellis, J. T., Conway, T., and Francey, R. J.: Global

941 carbon sinks and their variability inferred from atmospheric O-2 and delta C-13, Science, 287, 2467-

942 2470, 2000.

943 Bender, M. L., Tans, P. P., Ellis, J. T., Orchardo, J., and Habfast, K.: A High-Precision Isotope Ratio

944 Mass-Spectrometry Method for Measuring the O-2 N-2 Ratio of Air, Geochim Cosmochim Ac, 58,

945 4751-4758, 1994.

946 Berhanu, T. A., Satar, E., Schanda, R., Nyfeler, P., Moret, H., Brunner, D., Oney, B., and Leuenberger,

947 M.: Measurements of greenhouse gases at Beromünster tall tower station in Switzerland, Atmos.

948 Meas. Tech. , 9, 2016.

949 Berhanu, T. A., Szidat, S., Brunner, D., Satar, E., Schanda, R., Nyfeler, P., Battaglia, M., Steinbacher,

950 M., Hammer, S., and Leuenberger, M.: Estimation of the fossil-fuel component in atmospheric CO_2

951 based on radiocarbon measurements at the Beromünster tall tower, Switzerland, Atmos. Chem.

952 Phys. Discuss., 2017, 1-33, 2017.

953 Crosson, E. R. J. A. P. B.: A cavity ring-down analyzer for measuring atmospheric levels of methane,

954 carbon dioxide, and water vapor, 92, 403-408, 2008.

955 Filges, A., Gerbig, C., Rella, C. W., Hoffnagle, J., Smit, H., Krämer, M., Spelten, N., Rolf, C., Bozóki, Z.,

956 Buchholz, B., and Ebert, V.: Evaluation of the IAGOS-Core GHG Package H2O measurements during

957 the DENCHAR airborne inter-comparison campaign in 2011, Atmos. Meas. Tech., 11, 5279–5297,

958 2018, https://doi.org/10.5194/amt-11-5279-2018. Gao, F., Zhang, X., Zhang, X., Wang, M., and Wang,

959 P.: Virtual electronic nose with diagnosis model for the detection of hydrogen and methane in breath

960 from gastrointestinal bacteria, 28-31 May 2017 2017, 1-3.

961 Gordon, E., Rothman, S., Hill, C., Kochanov, V., Tan, Y., Bernath, P., Birk, M., Boudon, V., Campargue,

962 A., Chance, K., Drouin, J., Flaud, J., Gamache, R. R., Hodges, J., Jacquemart, D., Perevalov, I., Perrin, A.,

963 Shine, P., Smith, M., Tennyson, J., Toon, G., Tran, H., Tyuterev, G., Barbe, A., Császár, G., Devi, M.,

964   Furtenbacher, T., Harrison, J., Hartmann, J., Jolly, A., Johnson, J., Karman, T., Kleiner, I., Kyuberis, A.

965   A., Loos, J., Lyulin, M., Massie, S., Mikhailenko, S., Moazzen-Ahmadi, N., Muller, S., Naumenko, O. V.,

966   Nikitin, A. V., Polyansky, O. L., Rey, M., Rotger, M., Sharpe, S., Sung, K., Starikova, E., Tashkun, S.,

967   Auwera, J., Wagner, G., Wilzewski, J., Wcisło, P., Yu, S., and Zak, E. J.: The HITRAN2016 molecular

968   spectroscopic database, 203, 3 - 69, 2017.

969   Goto, D., Morimoto, S., Ishidoya, S., Aoki, S., and Nakazawa, T.: Terrestrial biospheric and oceanic

970   CO_2 uptake estimated from long-term measurements of atmospheric CO_2 mole fraction, $\delta 13C$ and

971     $\delta(O_2/N_2)$ at Ny-Ålesund, Svalbard, Journal of Geophysical Research: Biogeosciences, doi:

972   10.1002/2017JG003845, 2017. n/a-n/a, 2017.

973   Gottlieb, K., Le, C. X., Wacher, V., Sliman, J., Cruz, C., Porter, T., and Carter, S.: Selection of a cut-off

974   for high- and low-methane producers using a spot-methane breath test: results from a large north

975   American dataset of hydrogen, methane and carbon dioxide measurements in breath, Gastroenterol

976   Rep, 5, 193-199, 2017.

977   Hartmann, J.-M., Boulet, C., and Robert, D.: Collisional Effects on Molecular Spectra, Elsevier Science,

978   2008.

979   Henne, S., Brunner, D., Folini, D., Solberg, S., Klausen, J., and Buchmann, B.: Assessment of

980   parameters describing representativeness of air quality in-situ measurement sites, Atmos. Chem.

981   Phys., 10, 3561-3581, 2010.

982   Hodges, J. T., Layer, H. P., Miller, W. W., and Scace, G. E.: Frequency-stabilized single-mode cavity

983   ring-down apparatus for high-resolution absorption spectroscopy, 75, 849-863, 2004.

984   Keeling, R. F.: Development of an Interferometric Oxygen Analyzer for Precise Measurement of the

985   Atmospheric O_2 Mole Fraction, UMI, 1988a.

986   Keeling, R. F.: Measuring correlations between atmospheric oxygen and carbon dioxide mole

987   fractions: A preliminary study in urban air, J Atmos Chem, 7, 153-176, 1988b.

988   Keeling, R. F. and Manning, A. C.: 5.15 - Studies of Recent Changes in Atmospheric O2 Content A2 -

989   Holland, Heinrich D. In: Treatise on Geochemistry (Second Edition), Turekian, K. K. (Ed.), Elsevier,

990   Oxford, 2014.

991   Keeling, R. F. and Shertz, S. R.: Seasonal and Interannual Variations in Atmospheric Oxygen and

992   Implications for the Global Carbon-Cycle, Nature, 358, 723-727, 1992.

993   Keeling, R. F., Stephens, B. B., Najjar, R. G., Doney, S. C., Archer, D., and Heimann, M.: Seasonal

994   variations in the atmospheric O-2/N-2 ratio in relation to the kinetics of air-sea gas exchange, Global

995   Biogeochem Cy, 12, 141-163, 1998.

996   Lamouroux, J., Sironneau, V., Hodges, J. T., and Hartmann, J. M.: Isolated line shapes of molecular

997   oxygen: Requantized classical molecular dynamics calculations versus measurements, Physical

998   Review A, 89, 042504, 2014.

999   Le Quéré, C., Andrew, R. M., Friedlingstein, P., Sitch, S., Pongratz, J., Manning, A. C., Korsbakken, J. I.,

1000   Peters, G. P., Canadell, J. G., Jackson, R. B., Boden, T. A., Tans, P. P., Andrews, O. D., Arora, V. K.,

1001   Bakker, D. C. E., Barbero, L., Becker, M., Betts, R. A., Bopp, L., Chevallier, F., Chini, L. P., Ciais, P.,

1002   Cosca, C. E., Cross, J., Currie, K., Gasser, T., Harris, I., Hauck, J., Haverd, V., Houghton, R. A., Hunt, C.

1003   W., Hurtt, G., Ilyina, T., Jain, A. K., Kato, E., Kautz, M., Keeling, R. F., Klein Goldewijk, K., Körtzinger, A.,

1004   Landschützer, P., Lefèvre, N., Lenton, A., Lienert, S., Lima, I., Lombardozzi, D., Metzl, N., Millero, F.,

1005   Monteiro, P. M. S., Munro, D. R., Nabel, J. E. M. S., Nakaoka, S. I., Nojiri, Y., Padín, X. A., Peregon, A.,

1006   Pfeil, B., Pierrot, D., Poulter, B., Rehder, G., Reimer, J., Rödenbeck, C., Schwinger, J., Séférian, R.,

1007   Skjelvan, I., Stocker, B. D., Tian, H., Tilbrook, B., van der Laan-Luijkx, I. T., van der Werf, G. R., van

1008   Heuven, S., Viovy, N., Vuichard, N., Walker, A. P., Watson, A. J., Wiltshire, A. J., Zaehle, S., and Zhu,

1009   D.: Global Carbon Budget 2017, Earth Syst. Sci. Data Discuss., 2017, 1-79, 2017.

1010   Machta, L. and Hughes, E.: Atmospheric Oxygen in 1967 to 1970, Science, 168, 3939, 1582-1584,

1011   1970.

1012   Manning, A.: Temporal variability of atmospheric oxygen from both continuos and measurements

1013   and a flask sampling network: tools for studying the global carbon cycle, Ph.D. Ph.D., University of

1014   California, San Diego, San Diego, Calofornia, USA, 2001.

1015   Manning, A. C. and Keeling, R. F.: Global oceanic and land biotic carbon sinks from the Scripps

1016   atmospheric oxygen flask sampling network, Tellus B, 58, 95-116, 2006.

1017   Manning, A. C., Keeling, R. F., and Severinghaus, J. P.: Precise atmospheric oxygen measurements

1018   with a paramagnetic oxygen analyzer, Global Biogeochem Cy, 13, 1107-1115, 1999.

1019   Marrero, T. R. and Mason, E. A.: Gaseous Diffusion Coefficients, Journal of Physical and Chemical

1020   Reference Data 1, 3, 1972.

1021   Martin, N. A., Ferracci, V., Cassidy, N., and Hoffnagle, J. A. J. A. P. B.: The application of a cavity ring-

1022   down spectrometer to measurements of ambient ammonia using traceable primary standard gas

1023   mixtures, 122, 219, 2016.

1024   Mckay, L. F., Eastwood, M. A., and Brydon, W. G.: Methane Excretion in Man - a Study of Breath,

1025   Flatus, and Feces, Gut, 26, 69-74, 1985.

1026   Nevison, C. D., Keeling, R. F., Kahru, M., Manizza, M., Mitchell, B. G., and Cassar, N.: Estimating net

1027   community production in the Southern Ocean based on atmospheric potential oxygen and satellite

1028   ocean color data, Global Biogeochem Cy, 26, 2012.

1029   Oney, B., Henne, S., Gruber, N., Leuenberger, M., Bamberger, I., Eugster, W., and Brunner, D.: The

1030   CarboCount CH sites: characterization of a dense greenhouse gas observation network, Atmos.

1031   Chem. Phys., 15, 11147-11164, 2015.

1032   Press, W. H., Teukolsky, S. A., Vetterling, W. T., and Flannery, B. P.: Numerical Recipes 3rd Edition:

1033   The Art of Scientific Computing, Cambridge Printing Press, Cambridge, England, 1986.

1034   Press, W. H., Teukolsky, S. A., Vetterling, W. T., and Flannery, B. P.: Numerical recipes in C: the art of

1035   scientific computing, Cambridge University Press, London, 1992.

1036 Ryter, S. W. and Choi, A. M. K.: Carbon monoxide in exhaled breath testing and therapeutics, J Breath

1037 Res, 7, 2013.

1038 Satar, E., Berhanu, T. A., Brunner, D., Henne, S., and Leuenberger, M.: Continuous CO2/CH4/CO

1039 measurements (2012–2014) at Beromünster tall tower station in Switzerland, Biogeosciences, 13,

1040 2623-2635, 2016.

1041 Schibig, M. F., Steinbacher, M., Buchmann, B., van der Laan-Luijkx, I. T., van der Laan, S., Ranjan, S.

1042 and Leuenberger, M. C,: Comparison of continuous in situ CO2 observations at Jungfraujoch using

1043 two different measurement techniques, Atmospheric Measurement Techniques

1044 , 8, 57-68, 10.5194/amt-8-57-2015, 2015.

1045 Severinghaus, J. P.: Studies of the terresterial O2 and carbon cycles in sand dune gases and in

1046 Biosphere Doctoral Ph.D., Columbia University, New York, USA, 1995.

1047 Steig, E. J., Gkinis, V., Schauer, A. J., Schoenemann, S. W., Samek, K., Hoffnagle, J., Dennis, K. J., and

1048 Tan, S. M.: Calibrated high-precision ^{17}O-excess measurements using cavity ring-down

1049 spectroscopy with laser-current-tuned cavity resonance, Atmos. Meas. Tech., 7, 2014.

1050 Stephens, B. B., Bakwin, P. S., Tans, P. P., Teclaw, R. M., and Baumann, D. D.: Application of a

1051 differential fuel-cell analyzer for measuring atmospheric oxygen variations, J Atmos Ocean Tech, 24,

1052 82-94, 2007.

1053 Sturm, P., Leuenberger, M., Valentino, F.L., Lehmann, B. and B. Ihly: Measurements of CO_2, its stable

1054 isotopes, O_2/N_2, and ^{222}Rn at Bern, Switzerland, *Atmospheric Chemistry and Physics*, *6*, 1991-2004,

1055 2006.

1056 Tan, Y., Kochanov, R.V., Rothman, L., and Gordon, I.E.:Introduction of water-vapor broadening

1057 coefficients and their temeprature dependence exponents into the HITRAN database, Part 1: CO2,

1058 N2O, CO, CH4, O2, NH3, and H2S, Submitted to Journal of Geophysical Research Atmospheres, 2019,

1059 arXiv:1906.01475 .

1060   Tennyson, J., Bernath, P. F., Campargue, A., Császár, A. G., Daumont, L., Gamache, R. R., Hodges, J. T.,

1061   Lisak, D., Naumenko, O. V., Rothman, L. S., Tran, H., Zobov, N. F., Buldyreva, J., Boone, C. D., De Vizia,

1062   M. D., Gianfrani, L., Hartmann, J.-M., McPheat, R., Weidmann, D., Murray, J., Ngo, N. H., and

1063   Polyansky, O. L.: Recommended isolated-line profile for representing high-resolution spectroscopic

1064   transitions (IUPAC Technical Report), 86, 1931–1943, 2014.

1065   Tohjima, Y.: Method for measuring changes in the atmospheric O-2/N-2 ratio by a gas

1066   chromatograph equipped with a thermal conductivity detector, J Geophys Res-Atmos, 105, 14575-

1067   14584, 2000.

1068   Tran, H., Turbet, M., Hanoufa, S., Landsheere, X., Chelin, P., Ma, Q., Hartmann, J.: The CO2–

1069   broadened H2O continuum in the 100–1500 cm-1 region: Measurements, predictions and empirical

1070   model, Journal of Quantitative Spectroscopy and Radiative Transfer, 230, 75-80, 2019.

1071   Valentino, F. L., Leuenberger, M., Uglietti, C., and Sturm, P.: Measurements and trend analysis of O2,

1072   CO2 and δ13C of CO2 from the high altitude research station Junfgraujoch, Switzerland — A

1073   comparison with the observations from the remote site Puy de Dôme, France, Sci Total Environ, 391,

1074   203-210, 2008.

1075   Varghese, P. L. and Hanson, R. K.: Collisional narrowing effects on spectral line shapes measured at

1076   high resolution, Appl. Opt., 23, 2376-2385, 1984.

1077   Wójtewicz, S., Cygan, A., Masłowski, P., Domysławska, J., Wcisło, P., Zaborowski, M., Lisak, D.,

1078   Trawiński, R. S., and Ciuryło, R.: Spectral line-shapes of oxygen B-band transitions measured with

1079   cavity ring-down spectroscopy, Journal of Physics: Conference Series, 548, 012028, 2014.

1080   Wolf, P. G., Parthasarathy, G., Chen, J., O'Connor, H. M., Chia, N., Bharucha, A. E., and Gaskins, H. R.:

1081   Assessing the colonic microbiome, hydrogenogenic and hydrogenotrophic genes, transit and breath

1082   methane in constipation, Neurogastroent Motil, 29, 2017.

1083   Zellweger, C., Forrer, J., Hofer, P., Nyeki, S., Schwarzenbach, B., Weingartner, E., Ammann, M., and

1084   Baltensperger, U.: Partitioning of reactive nitrogen (NO_y) and dependence on

1085   meteorological conditions in the lower free troposphere, Atmos. Chem. Phys., 3, 779-796, 2003.

1086